

Cosmological constraints from cosmic shear two-point correlation functions with HSC survey first-year data

Takashi HAMANA^{1,2}, Masato SHIRASAKI¹, Satoshi MIYAZAKI^{1,2}, Chiaki HIKAGE³, Masamune OGURI^{4,5,3}, Surhud MORE^{6,3}, Robert ARMSTRONG⁷, Alexie LEAUTHAUD⁸, Rachel MANDELBAUM⁹, Hironao MIYATAKE^{10,11,3,12}, Atsushi J. NISHIZAWA^{10,11}, Melanie SIMET^{13,12}, Masahiro TAKADA³, Hiroaki AIHARA⁵, James BOSCH¹⁴, Yutaka KOMIYAMA^{1,2}, Robert LUPTON¹⁴, Hitoshi MURAYAMA^{3,15,16}, Michael A. STRAUSS¹⁴ and Masayuki TANAKA¹

¹National Astronomical Observatory of Japan, Mitaka, Tokyo 181-8588, Japan

²The Graduate University for Advanced Studies, SOKENDAI, Mitaka, Tokyo 181-8588, Japan

³Kavli Institute for the Physics and Mathematics of the Universe (Kavli IPMU, WPI), University of Tokyo, Chiba 277-8582, Japan

⁴Research Center for the Early Universe, University of Tokyo, Tokyo 113-0033, Japan

⁵Department of Physics, University of Tokyo, Tokyo 113-0033, Japan

⁶The Inter-University Center for Astronomy and Astrophysics, Post bag 4, Ganeshkhind, Pune, 411007, India

⁷Lawrence Livermore National Laboratory, Livermore, CA 94551, USA

⁸University of California Santa Cruz, 1156 High St., Santa Cruz, CA 95064, USA

⁹McWilliams Center for Cosmology, Department of Physics, Carnegie Mellon University, Pittsburgh, PA 15213, USA

¹⁰Institute for Advanced Research, Nagoya University, Nagoya 464-8602, Aichi, Japan

¹¹Division of Particle and Astrophysical Science, Graduate School of Science, Nagoya University, Nagoya 464-8602, Aichi, Japan

¹²Jet Propulsion Laboratory, California Institute of Technology, Pasadena, CA 91109, USA

¹³University of California, Riverside, 900 University Avenue, Riverside, CA 92521, USA

¹⁴Department of Astrophysical Sciences, Princeton University, 4 Ivy Lane, Princeton, NJ 08544, USA

¹⁵Department of Physics and Center for Japanese Studies, University of California, Berkeley, CA 94720, USA

¹⁶Theoretical Physics Group, Lawrence Berkeley National Laboratory, MS 50A-5104, Berkeley, CA 94720, USA

Received 2019 June 14; Accepted 2019 November 21

Abstract

We present measurements of cosmic shear two-point correlation functions (TPCFs) from Hyper Suprime-Cam Subaru Strategic Program (HSC SSP) first-year data, and derived cosmological constraints based on a blind analysis. The HSC first-year shape catalog is divided into four tomographic redshift bins ranging from $z = 0.3$ to 1.5 with equal widths of $\Delta z = 0.3$. The unweighted galaxy number densities in each tomographic bin are 5.9, 5.9, 4.3, and 2.4

arcmin⁻² from the lowest to highest redshifts, respectively. We adopt the standard TPCF estimators, ξ_{\pm} , for our cosmological analysis, given that we find no evidence of the significant B-mode shear. The TPCFs are detected at high significance for all ten combinations of auto- and cross-tomographic bins over a wide angular range, yielding a total signal-to-noise ratio of 19 in the angular ranges adopted in the cosmological analysis, $7' < \theta < 56'$ for ξ_+ and $28' < \theta < 178'$ for ξ_- . We perform the standard Bayesian likelihood analysis for cosmological inference from the measured cosmic shear TPCFs, including contributions from intrinsic alignment of galaxies as well as systematic effects from PSF model errors, shear calibration uncertainty, and source redshift distribution errors. We adopt a covariance matrix derived from realistic mock catalogs constructed from full-sky gravitational lensing simulations that fully account for survey geometry and measurement noise. For a flat Λ cold dark matter model, we find $S_8 \equiv \sigma_8 \sqrt{\Omega_m/0.3} = 0.804^{+0.032}_{-0.029}$, and $\Omega_m = 0.346^{+0.052}_{-0.100}$. We carefully check the robustness of the cosmological results against astrophysical modeling uncertainties and systematic uncertainties in measurements, and find that none of them has a significant impact on the cosmological constraints.

Key words: cosmology: observations — dark matter — cosmological parameters — large-scale structure of universe

1 Introduction

The Λ cold dark matter (Λ CDM) model is now considered to be the standard theoretical framework for the expansion history of the Universe and for cosmic structure formation. The standard Λ CDM model is described by only a handful of cosmological parameters. Measuring values of the cosmological parameters, as well as checking their consistency between different cosmological observations, is one of the most important goals of modern cosmology. Multiple probes, such as the cosmic microwave background (CMB; e.g., Hinshaw et al. 2013; Planck Collaboration et al. 2016, 2018), high redshift type-Ia supernovae (e.g., Suzuki et al. 2012; Betoule et al. 2014, and Weinberg et al. 2013 for a review), baryon acoustic oscillations (BAOs; e.g., Anderson et al. 2014; Alam et al. 2017), and weak lensing as described in detail below, have been utilized for this purpose. Different methods probe different cosmic epochs through a measurement of the growth of cosmic structure formation and/or the distance-redshift relation of the Universe. In addition, the methods have different parameter degeneracies and are affected by different systematic effects. For these reasons, it is common practice to combine multiple probes to infer tighter and more reliable cosmological constraints. More importantly, if a discordance between cosmological constraints from different probes is found, it may indicate physics beyond the Λ CDM model. Therefore it is of fundamental importance to infer improved cosmological constraints from each probe. This is exactly the purpose of this study, which uses weak lensing observations from the HSC SSP.

Weak lensing is one of the most powerful tools for cosmology, as it provides a unique means to study the matter distribution in the Universe. The cosmic shear is the coherent distortion of the shapes of distant galaxies caused by the gravitational lensing of intervening large-scale structures, including the dark matter component. Statistical measures of cosmic shear, such as the two-point correlation function (TPCF) or the power spectrum, depend both on the time evolution of the cosmic structures and on the cosmic expansion history, and thus serve as a unique cosmological probe. They probe the large-scale, linear to weakly non-linear, matter power spectrum at relatively recent epochs ($z < 1$), and thus are most sensitive to the normalization of matter fluctuation (σ_8) and the mean matter density parameter (Ω_m) (Jain & Seljak 1997). Because of the degeneracy between these two parameters, the combination $S_8 = \sigma_8(\Omega_m/0.3)^\alpha$ with a degeneracy direction of $\alpha \sim 0.5$ is commonly used to quantify the constraints from cosmic shear.

Cosmological constraints from cosmic shear are improved primarily by increasing the survey volume as well as the number density of source galaxies, along with a proper control of systematic effects. Currently, three wide-field imaging surveys that will each eventually cover over 1000 square degrees are underway; the Dark Energy Survey (DES, Dark Energy Survey Collaboration et al. 2016), the Kilo-Degree survey (KiDS, de Jong et al. 2013), and the Hyper Suprime-Cam Subaru Strategic Program (hereafter the HSC survey; Aihara et al. 2018b). All three projects have published initial cosmic shear analyses with early data, yielding 4–8 percent constraints on S_8 (Troxel

et al. 2018; Hildebrandt et al. 2017; Köhlinger et al. 2017; Hildebrandt et al. 2018; Hikage et al. 2019). They also demonstrated that none of the systematic effects examined in the papers seriously affected the resulting constraints.

Among the three surveys, the unique advantage of the HSC survey is its higher galaxy number density¹ of 16.5 arcmin^{-2} compared to that of DES (5.14 arcmin^{-2}) and KiDS (6.85 arcmin^{-2}), due to the combination of its depth (5σ point-source depth of the Wide layer of $i \sim 26 \text{ AB mag}$) and excellent image quality (typical i -band seeing of $0.''58$, Aihara et al. 2018a; Mandelbaum et al. 2018a). Hikage et al. (2019) measured the tomographic cosmic shear power spectra using the HSC survey first-year data over 137 deg^2 . They selected galaxies from the HSC first-year weak lensing shear catalog (Mandelbaum et al. 2018a) with photometric redshifts (Tanaka et al. 2018) ranging from 0.3 to 1.5, and divided them into four tomographic redshift bins with equal widths of $\Delta z = 0.3$. Even the highest redshift tomographic bin contains 2.0 galaxies per arcmin^2 . They detected cosmic shear power spectra with high signal-to-noise ratios (SN) of $SN = 4.9, 9.2, 12.3,$ and 11.5 for auto-power spectra of each tomographic bin (from the lowest to highest redshift) and $SN = 15.6$ for combined auto- and cross-power spectra.

In this paper, we present the cosmic shear TPCFs measured from the HSC survey first-year data, and derive cosmological constraints with them. We use the same data set as that used in Hikage et al. (2019), but use a completely different analysis scheme, namely the real-space TPCFs instead of Fourier-space power spectra, using an independent cosmological inference pipeline. In principle, those two estimates provide almost the same information, but different treatments of actual observational effects, such as discrete galaxy sampling and the correction of the irregular survey geometry, which can affect the measured signal and the cosmological inference in different ways. Also, the two approaches have different noise properties and different sensitivities to systematic effects, and are sensitive to different scales. Therefore this study provides an important cross-check of the robustness of the Fourier-space analysis by Hikage et al. (2019). Furthermore, our analysis indicates that our TPCF analysis probes a slightly different range of multipole from that used in Hikage et al. (2019), and therefore contains some complementary cosmological information.

The structure of this paper is as follows. In Section 2, we briefly summarize the HSC survey first-year shear catalog and the photometric redshift data used in this study.

¹ The number densities given in this paragraph are the effective number density of galaxies used for cosmic shear analyses defined in Chang et al. (2013) and are taken from Table 1 and 2 of Hikage et al. (2019).

We also describe our blind analysis scheme. In Section 3, we describe the method to measure the TPCFs of the cosmic shear, and present our measurements. We also present TPCFs of the measured shapes of stars and residuals between those shapes and the point spread function (PSF) model, which allow us to estimate the residual systematics in the cosmic shear TPCFs. In Section 4, we summarize model ingredients for the cosmic shear TPCFs and covariance. Our method for cosmological inference is described in Section 5 along with our methods to take into account various systematics in our cosmological analysis. Our cosmological constraints and tests for systematics are presented in Section 6. Finally, we summarize and discuss our results in Section 7. In Appendix 2, we describe the impact of the PSF leakage and the residual PSF model error on the measurement of shear TPCFs. In Appendix 3, we present E/B-mode TPCFs measured from the HSC survey data. In Appendix 4, we describe mock simulation data that are used to derive the covariance matrix and to test our cosmological inference pipeline. In Appendix 5, the difference of the information content in the measured cosmic shear statistics between this study and Hikage et al. (2019) is examined. In Appendix 6, we discuss a possible impact of an error in the outlier fraction of galaxy redshift distributions on cosmological constraints on.

Throughout this paper we quote 68% credible intervals for parameter uncertainties unless otherwise stated.

2 HSC survey data

In this section, we briefly summarize the HSC survey products used in this study. Hikage et al. (2019) describe the dataset we use in detail; here we focus on those aspects that are directly relevant to this study. We refer the readers to Aihara et al. (2018b) for an overview of the HSC survey and survey design, Aihara et al. (2018a) for the first public data release, Miyazaki et al. (2018); Komiyama et al. (2018); Kawanomoto et al. (2018); Furusawa et al. (2018) for the performance of the HSC instrument itself, Bosch et al. (2018) for the optical imaging data processing pipeline used for the first-year data, Mandelbaum et al. (2018a) for the first-year shape catalog, Mandelbaum et al. (2018b) for the calibration of galaxy shape measurements with image simulations, and Tanaka et al. (2018) for photometric redshifts derived for the first data.

2.1 HSC first-year shape catalog

We use the HSC first-year shape catalog (Mandelbaum et al. 2018a), in which the shapes of galaxies are estimated on the i -band coadded image using the re-Gaussianization

PSF correction method (Hirata & Seljak 2003). Only galaxies that pass our selection criteria are contained in the catalog. Among others, the four major criteria for galaxies to be selected are,

- (1) *full-color and full-depth cut*: the object should be located in regions reaching approximately full survey depth in all five (*grizy*) broad bands,
- (2) *magnitude cut*: *i*-band *c*model magnitude (corrected for extinction) should be brighter than 24.5 AB mag,
- (3) *resolution cut*: the galaxy size normalized by the PSF size defined by the re-Gaussianization method should be larger than a given threshold of `ishape_hsm_regauss_resolution` ≥ 0.3 ,
- (4) *bright object mask cut*: the object should not be located within the bright object masks.

See Table 4 of Mandelbaum et al. (2018a) for the full description of the selection criteria. As a result, the final weak lensing shear catalog covers 136.9 deg^2 , consisting of 6 disjoint regions (named XMM, GAMA09H, WIDE12H, GAMA15H, VVDS, and HECTOMAP) and contains $\sim 12.1\text{M}$ galaxies.

2.2 Photometric redshifts

Since spectroscopic redshifts have been obtained for only a small fraction of galaxies in the HSC shape catalog, we utilize photometric redshift (hereafter photo- z) information to divide galaxies into tomographic redshift bins.

Utilizing the HSC five-band photometry, photo- z s were estimated with six independent codes, described in detail in Tanaka et al. (2018). Three of the six photo- z 's used the PSF-matched aperture photometry (called the **afterburner** photometry; see Aihara et al. 2018a), which we adopt in this study: They are (1) an empirical polynomial fitting method (DEmP) (Hsieh & Yee 2014), (2) a neural network code (Ephor AB), and (3) a hybrid code combining machine learning with template fitting (FRANKEN-Z).

The accuracy of HSC photo- z 's were examined in detail in Tanaka et al. (2018), who concluded that HSC photo- z 's (z_p) are most accurate at $0.2 \lesssim z_p \lesssim 1.5$. Given the smaller lensing signals for lower redshift galaxies, we set the redshift range of our cosmic shear analysis from 0.3 to 1.5. We adopt the **best** estimate of Ephor AB for the point estimator of photo- z 's to define tomographic bins. Specifically, we select galaxies with the point estimator being within that redshift range, and divide them into four tomographic redshift bins with equal redshift width of $\Delta z = 0.3$, again based on the point estimator. After the redshift cut, the final number of galaxies used in this study is ~ 9.0 million, which are split into four tomographic bins, containing

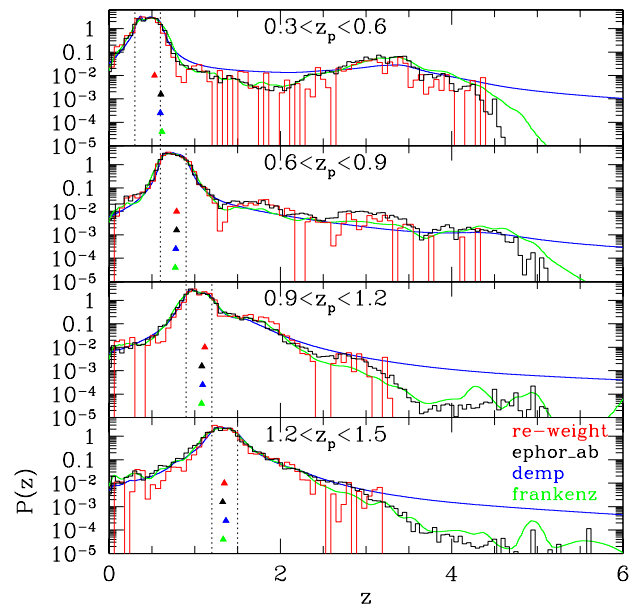


Fig. 1. Histograms show galaxy redshift distributions for the four tomographic redshift bins; $0.3 < z < 0.6$, $0.6 < z < 0.9$, $0.9 < z < 1.2$, and $1.2 < z < 1.5$, from the top to bottom panels, respectively. The triangles show the mean redshift of each redshift distribution. The vertical dotted lines show the boundaries of the four tomographic bins. The redshift distributions are computed up to $z = 6$. Different colors indicate different methods: The COSMOS-reweighted method (red) is our principal method. In order to test the robustness of our results against uncertainties in the redshift distributions, we will use stacked- $P(z)$ with three photo- z methods, Ephor AB (black), DEmp (blue), and FRANKEN-Z (green). Different binning for different methods originates from their different redshift resolutions, except for the COSMOS-reweighted method for which a three-times under-sampled binning is shown for clarity (the original resolution is $\Delta z = 0.02$).

2.8M, 2.8M, 2.1M, and 1.2M galaxies respectively from the lowest to highest redshift bins.

2.2.1 Redshift distribution of galaxies in each tomographic bin

Since the photo- z point estimator is a noisy estimator of the true redshifts of galaxies, the true redshift distribution of galaxies in individual tomographic bins must be separately and reliably estimated. We follow the methodology described in Hikage et al. (2019) to infer the true redshift distribution as well as to test the robustness of derived cosmological results against uncertainty in the adopted redshift distributions. They adopted the reweighting method based on the HSC's five-band photometry and COSMOS 30-band photo- z catalog (Ilbert et al. 2009; Laigle et al. 2016). We refer the readers to Section 5.2 of Hikage et al. (2019) and references therein for a full detail of the method. Here we only present the derived redshift distributions as the red histograms in Figure 1, which are the same as those used in Hikage et al. (2019). The distributions computed to $z = 6$. We use them as our fiducial redshift distributions

in our cosmological analysis. In our model description in Section 4, these redshift distributions are denoted as $p^a(z)$, where $a = 1 - 4$ runs over the four tomographic bins. We note that for the lowest tomographic bin, the mean redshift shown by the red triangle looks not to match up with the histograms. This is due to outliers located at higher redshifts. The 3σ clipped mean redshifts are summarized in Table 4 of Hikage et al. (2019). For the lowest bin, the clipped mean is $z = 0.44$ which is very close to the median redshift of $z = 0.43$.

We also infer the stacked photo- z probability distribution functions (PDFs), which are obtained by stacking the full PDFs of photo- z 's for individual galaxies ($P_j(z)$) with their shear weight (w_j), $p^a(z) = \sum_j w_j P_j(z) / \sum_j w_j$, where the summation runs over all galaxies in individual tomographic bins. The stacked photo- z PDFs for the three photo- z methods are shown in the three bottom panels of Figure 1. Since stacking $P_j(z)$ is not a mathematically sound way to infer the true redshift distribution (see Section 5.2 of Hikage et al. 2019), we do not adopt the stacked $p(z)$ as a fiducial choice, but use it merely for testing the impact of redshift distribution uncertainties in Section 6.3.4.

2.3 Weak lensing shear estimation

The HSC shape catalog described in Section 2.1 contains all the basic parameters needed to estimate the weak lensing shear with the re-Gaussianization method, including corrections for biases. The following five sets of parameters for each galaxy are directly relevant to this study; (1) the two-component distortion, $\mathbf{e} = (e_1, e_2)$, which represents the shape of each galaxy image, (2) shape weight, w , (3) intrinsic shape dispersion per component, e_{rms} , (4) multiplicative bias, m , and (5) additive bias, (c_1, c_2) . Following Appendix A of Mandelbaum et al. (2018a), an estimator for the shear is obtained for each galaxy as

$$\hat{\gamma}_i = \frac{1}{1 + \bar{m}} \left[\frac{e_i}{2\mathcal{R}} - c_i \right], \quad (1)$$

with the weighted-average multiplicative bias factor,

$$\bar{m} = \frac{\sum_i w_i m_i}{\sum_i w_i}, \quad (2)$$

and the shear responsivity \mathcal{R} representing the response of the distortion to a small shear (Kaiser et al. 1995; Bernstein & Jarvis 2002) given by

$$\mathcal{R} = 1 - \frac{\sum_i w_i e_{\text{rms}}^2}{\sum_i w_i}. \quad (3)$$

In the above expressions, the subscript i denotes each galaxy, and the summation is taken over all galaxies in each tomographic redshift bin.

2.3.1 Selection bias

In addition to the shear calibration mentioned above, which is based on the full galaxy sample in the shape catalog, we take account of the additional multiplicative biases arising from the tomographic redshift galaxy selection. To do so, we follow Hikage et al. (2019) and we refer the readers to the paper and references therein for details. In short, there are two sources of biases: One is the selection bias that is due to the difference in galaxy size distributions for different tomographic samples. The other is the correction to the shear responsivity due to the dependence of the intrinsic ellipticity variation on redshift (see subsection 5.3 of Mandelbaum et al. (2018b) for details). Both biases vary with the tomographic bins. The former is denoted by m_{sel}^a and the latter is denoted by m_R^a , where the superscript a labels the tomographic bin. As we use exactly the same data set as that used in Hikage et al. (2019) with the same tomographic binning, we adopt the same values of those biases given in Table 3 of Hikage et al. (2019). We apply these corrections to the *theoretical prediction* of cosmic shear TPCFs (see Section 4.3) as $\xi_{\pm}^{ab}(\theta) \rightarrow (1 + m_{\text{sel}}^a + m_R^a)(1 + m_{\text{sel}}^b + m_R^b)\xi_{\pm}^{ab}(\theta)$.

2.4 Blinding

In order to avoid confirmation bias, we perform our cosmological analysis in a blind fashion. The HSC weak lensing team defined blinding and unblinding procedures, and agreed that they must be followed in cosmological analysis of the weak lensing data (see Section 3.2 of Hikage et al. 2019 for the overall description). Here we give a brief overview of the blinding scheme we adopt for our analysis.

We use a two-level blinding scheme similar to Hikage et al. (2019). The first is a catalog-level blinding, while the second is the analysis-level blinding which is adopted during the cosmological analysis. At the catalog-level, we blind the real shear values by modifying the multiplicative bias as

$$m_{\text{cat}}^i = m_{\text{true}} + dm_1^i + dm_2^i, \quad (4)$$

where m_{true} denotes the array of true multiplicative bias values in the HSC shape catalog for each galaxy, and the index i runs from 0 to 2 and denotes the three different shear catalog versions. There are multiple cosmological analyses that are being conducted by the HSC team, each with different analysis leads. Each analysis lead receives a separate set of three catalogs. The analysis team carried out the same analysis for all the three catalogs. The values of dm_1^i are different for each of the three catalogs as well as for each analysis team, and are encrypted. Only the PI of each analysis team can decrypt them, and this term

is removed before performing the analysis. This prevents an accidental comparison of blinded catalogs by another analysis team. The values of dm_2^i are different for the three catalogs and are encrypted by a public key from a person designated “blinder-in-chief”. Only one of the dm_2^i values is zero. These values can be decrypted only by the blinder-in-chief once all the conditions for unblinding have been met (see below).

The analysis-level blinding procedure involves blinding of the best-fit values of the inferred cosmological constraints. All cosmological constraint plots were plotted with shifted values of cosmological parameters (\mathbf{p}) such that $\mathbf{p}_{\text{blind}} = \mathbf{p} - \mathbf{p}_{\text{best}}$, before inspecting the derived constraints for systematics tests.

We laid down two conditions for unblinding: (1) the passing of sanity checks of the analysis software and the treatment of systematic effects, and (2) validation of analysis choices for cosmic shear TPCFs and studies of their impact on the cosmological constraints, which we describe in the following sections. After the final unblinding, we did not change the analysis setup in any way, and we report the cosmological constraints as at the time of unblinding. We unblind in stages; the first analysis-level unblinding was removed about a month and a half before the catalog-level unblinding. Three versions of the paper, corresponding to the analysis from each of the three blinded catalogs, were written up prior to the catalog-level unblinding. (Note that this step differs from the unblinding process of Hikage et al. 2019, they did the catalog-level unblinding soon after the first analysis-level unblinding, then wrote up the paper based on the true catalog.) Then after the catalog-level unblinding and before submission to the journal, the paper based on the true catalog underwent internal review from the HSC collaboration. No change in the results was made at the internal reviewing stage.

It should be noted that although we analyzed the three blind catalogs, we used the same covariance matrix derived from realistic mock catalogs which were generated using the true shape catalog (see Section 4.4 for details). As a result, derived best-fit χ^2 values for three blind catalogs were different reflecting the added dm_1^i to each catalog. To be specific, for our fiducial analysis setup (see Section 5), derived best-fit χ^2 values for the true catalog was found to be 162.3 for the effective degree-of-freedom of 167 (see Section 5.2.4), whereas χ^2 for two false catalogs were 114.0 and 116.0 for dm_1^i values of 0.08491 and 0.08004, respectively (note that those numbers were generated based on a random number generator and were very close each other by an accidental chance). It is true that the χ^2 values were a possible indication of which was the true catalog, though the true catalog does not necessarily

give the most reasonable χ^2 value. It is important to note that before unblinding the analysis-level blinding, we had no idea about inferred cosmological parameter values as the best-fit values were blinded, and after unblinding the analysis-level blinding, we did not change any analysis setup. The catalog-level blinding might not work as designed because of our use of the same covariance matrix. Even so, the analysis-level blinding worked to avoid the confirmation bias.

3 Measurements from the HSC survey data

In this section, we present our measurements of tomographic cosmic shear TPCFs from the HSC first-year data. In addition, we present measurements of the auto- and cross-TPCFs of the shapes of PSFs and the difference between the shapes of the PSF model and of stars, which we use to quantify residual systematics in our cosmic shear TPCF measurements.

3.1 Cosmic shear TPCFs

We adopt the standard estimates of cosmic shear TPCFs, $\xi_{\pm} = \langle \gamma_t \gamma_t \rangle \pm \langle \gamma_{\times} \gamma_{\times} \rangle$, where the tangential (t) and cross (\times) components of shear are defined with respect to the direction connecting a pair of galaxies under consideration. They can be estimated for two tomographic redshift bins a and b as

$$\hat{\xi}_{\pm}^{ab}(\theta) = \frac{\sum_{ij} w_i w_j [\hat{\gamma}_{i,t}^a(\vec{\theta}_i) \hat{\gamma}_{j,t}^b(\vec{\theta}_j) \pm \hat{\gamma}_{i,\times}^a(\vec{\theta}_i) \hat{\gamma}_{j,\times}^b(\vec{\theta}_j)]}{\sum_{ij} w_i w_j}, \quad (5)$$

where the summation runs over pairs of galaxies with their angular separation $\theta = |\vec{\theta}_i - \vec{\theta}_j|$ within an interval $\Delta\theta$ around θ .

For the measurement of the TPCFs themselves, we used the public software **Athena**² (Schneider et al. 2002). A total of 31 bins with equal logarithmic bin-widths of $\Delta \log_{10} \theta = 0.1$ are chosen with central θ ranging from $10^{-0.5} \simeq 0.316$ arcmin to $10^{2.5} \simeq 316$ arcmin, although only a subset of these angular bins are used in our cosmological analyses as described in Section 5.1. As described in Section 2.1, the HSC first-year shape catalog consists of 6 disjoint fields. Since gaps between fields are more than 20 degrees, we first compute the denominator and numerator of equation (5) for each field and then sum up each term separately for the final results. Overall, we have non-zero detections in most angular bins between $\theta \sim 1'$ and $\sim 100'$.

² <http://www.cosmostat.org/software/athena>

3.2 TPCFs of shapes of PSF and residuals

The PSF anisotropy induces additional deformation in galaxy shapes, which the shear estimation algorithm must correct for (see Mandelbaum 2018, for a review). However, in the case of the re-Gaussianization PSF correction method, a small residual in the correction for PSF anisotropy is unavoidable for two reasons: imperfect measurements and/or modeling of PSFs, and the correction error for PSF from galaxy images, an effect referred to as PSF leakage. In fact, systematic tests of the HSC first-year shape catalog showed small residual correlations between galaxy shears and PSF shapes (Mandelbaum et al. 2018a), which may bias the cosmic shear TPCFs and our cosmological analysis.

Here we outline our scheme to correct for these systematics. We follow the simple model used by Hikage et al. (2019) (see also Troxel et al. 2018), in which PSF residuals are assumed to be added to the shear linearly

$$\gamma^{\text{SYS}} = \alpha_{\text{psf}} \gamma^p + \beta_{\text{psf}} \gamma^q, \quad (6)$$

where γ^p is the shear³ of the shape of the model PSF, and γ^q is the difference in shears between the PSF model and the true PSF, as estimated from the shapes of individual stars, γ^* , i.e., $\gamma^q = \gamma^p - \gamma^*$. The first and second terms of the right hand side of equation (6) represent the residual PSF effects from the deconvolution error and the imperfect PSF model mentioned above, respectively. With these terms added to the measured shear $\hat{\gamma}$, the contributions from these terms to observed TPCFs are written as

$$\hat{\xi}_{\text{psf},\pm}(\theta) = \alpha_{\text{psf}}^2 \xi_{\pm}^{pp}(\theta) + 2\alpha_{\text{psf}}\beta_{\text{psf}} \xi_{\pm}^{pq}(\theta) + \beta_{\text{psf}}^2 \xi_{\pm}^{qq}(\theta), \quad (7)$$

where ξ_{\pm}^{pp} and ξ_{\pm}^{qq} represent the auto-TPCFs of γ^p and γ^q , respectively, and ξ_{\pm}^{pq} are the cross-TPCFs of γ^p and γ^q . Those TPCFs are computed using stars that were reserved from the PSF estimation (see Bosch et al. 2018, for details). In the HSC data reduction pipeline, stars used for PSF measurement/modeling are selected based on the distribution of high- S/N objects with stellar sizes. About 80% of selected stars are used for the PSF measurement and its modeling (those are flagged as `icalib_psf_used=True` in the HSC 1st-year shape catalog), while the remaining stars are *reserved* for cross-validation of the PSF modeling, which we use to compute the TPCFs. The measured TPCFs are presented in Appendix 2. An estimation of the proportionality factors α_{psf} and β_{psf} is given in Appendix 2, in which we find $\alpha_{\text{psf}} \sim 0.03$ and $\beta_{\text{psf}} \sim -1.4$. Therefore, given the amplitude of the measured TPCFs,

$\hat{\xi}_{\text{psf},+}$ can be as large as $\sim 10^{-6}$ at $\theta \sim 10'$. We correct this effect by adding the term, equation (7), to the *theoretical model* of the cosmic shear TPCFs (see Section 4.3). Our treatment of this systematic effect in the cosmological analysis is described in Section 5.2.3. This residual PSF effect on ξ_- is much smaller than that on ξ_+ (see Appendix 2), so we do not apply that correction to ξ_- .

4 Models of the cosmic shear TPCFs and covariance matrix

In this section, we summarize models for the measured cosmic shear TPCFs, consisting of two major components, the cosmic shear arising from the gravitational lensing effect by large-scale structures (see Kilbinger 2015, for a review) and the intrinsic alignment of galaxy shape (see Troxel & Ishak 2015; Kirk et al. 2015, for reviews). In practice, the measured cosmic shear TPCFs are also affected by systematics, such as the shear calibration error and residual PSF error and/or modeling, which we also summarize in this section. In addition, we describe our model of covariance matrix used for the cosmological analysis.

4.1 Cosmic shear TPCFs

The cosmic shear TPCFs induced by the gravitational lensing effect are related to the cosmic shear power spectra as (see e.g., Kilbinger 2015, and references therein)

$$\xi_{\text{GG},\pm}^{ab}(\theta) = \frac{1}{2\pi} \int d\ell \ell J_{0,4}(\ell\theta) P_{\kappa}^{ab}(\ell), \quad (8)$$

where a and b refer to tomographic redshift bins and $J_{0,4}(x)$ is the zeroth-order (for ξ_+) or fourth-order (for ξ_-) Bessel function of the first kind. We note that in the above expression and in what follows we assume no B-mode shear because we find that the B-mode component of cosmic shear TPCFs is consistent with zero as shown in Appendix 3 (see also Hikage et al. 2019 from the power spectrum analysis of the B-mode shear). Using the flat-sky and the Limber approximations, the convergence power spectrum, $P_{\kappa}(\ell)$, is computed from the nonlinear matter power spectrum, $P_m^{NL}(k)$, as

$$P_{\kappa}^{ab}(\ell) = \int_0^{\chi_H} d\chi \frac{q^a(\chi)q^b(\chi)}{f_K^2(\chi)} P_m^{NL}\left(\frac{\ell}{f_K(\chi)}, \chi\right), \quad (9)$$

where χ is the comoving radial distance, χ_H is the comoving horizon distance, and $f_K(\chi)$ is the comoving angular distance. For the computation of the linear matter power spectrum, we use **CAMB** (Challinor & Lewis 2011). In order to model the nonlinear matter power spectrum, we employ the fitting function by Bird et al. (2012), which is based on the **halofit** model (Smith et al. 2003; Takahashi et al.

³“Shears” of stars and PSFs are converted from the measured distortion using the relation between them for intrinsically round objects ($\gamma = e/2$). See Mandelbaum et al. (2018a) for the definition of distortion of star images.

2012) but is modified so as to include the effect of non-zero neutrino mass. Finally, the lensing efficiency function, $q(\chi)$, is defined as

$$q^a(\chi) = \frac{3}{2}\Omega_m \left(\frac{H_0}{c}\right)^2 \int_{\chi}^{\chi_H} d\chi' p^a(\chi')(1+z) \frac{f_K(\chi)f_K(\chi, \chi')}{f_K(\chi')}, \quad (10)$$

where $p^a(\chi)$ denotes the redshift distribution of source galaxies in the a -th tomographic bin and is normalized so that $\int d\chi p^a(\chi) = 1$.

The dependence of cosmological parameters enters the cosmic shear TPCFs through the nonlinear matter power spectrum, the distance-redshift relation, and the normalization of the lensing efficiency function, equation (10). Since our cosmological analysis is limited to the flat Λ CDM model with non-zero neutrino mass, the relevant cosmological parameters are the density parameter of CDM (Ω_c), the density parameter of baryons (Ω_b), the Hubble parameter (h), the scalar amplitude of the linear matter power spectrum on $k = 0.05 \text{ Mpc}^{-1}$ (A_S), the scalar spectrum index (n_s), and the sum of neutrino masses ($\sum m_\nu$). The cosmological constant parameter is determined under the assumption of a flat Universe, $\Omega_\Lambda = 1 - \Omega_c - \Omega_b - \Omega_\nu$, where Ω_ν is the density parameter corresponding to neutrinos.

4.1.1 Effects of baryonic physics on the nonlinear matter power spectrum

It is well known that the evolution of the nonlinear matter power spectrum, especially on small scales, is affected by baryon physics such as gas cooling, star formation, and supernova and active galactic nuclei (AGN) feedbacks (Schaye et al. 2010; van Daalen et al. 2011; Mead et al. 2015; Hellwing et al. 2016; McCarthy et al. 2017; Springel et al. 2018; Chisari et al. 2018). Quantitative estimates of those effects have not yet converged, due to uncertainties in the implementation of sub-grid baryon physics in cosmological hydrodynamical simulations (White 2004; Zhan & Knox 2004; Jing et al. 2006; Semboloni et al. 2011; Osato et al. 2015).

We mitigate these effects of baryon physics in our cosmological analysis by not including the measurements of the TPCFs on small scales where the effects are significant (see Section 5.1). As a further check, we test their impact using an extreme model, the AGN feedback model by Harnois-Déraps et al. (2015) that is based on the cosmological hydrodynamical simulations of Schaye et al. (2010); van Daalen et al. (2011) (OverWhelming Large Simulations (OWLS)). We note that all of other predictions of the baryonic effects based on other state-of-the-art simulations including the EAGLE simulation (Hellwing et al. 2016), the IllustrisTNG simulations (Springel et al.

2018), and the Horizon set of simulations (Chisari et al. 2018) have a smaller effect on the matter power spectrum than the OWLS AGN feedback model we adopt in this study. However it should be noted that current baryonic simulation results do not necessarily span all potential real feedback models. We thus allow to vary the strength of feedback by introducing a parameter. We follow the methodology of Köhlinger et al. (2017), in which a modification of the dark matter power spectrum due to the AGN feedback is modeled by the fitting function derived by Harnois-Déraps et al. (2015), but an additional parameter (A_B) that controls the strength of the feedback is introduced (see Section 5.1.2 of Köhlinger et al. 2017, for the explicit expression). We note that Hikage et al. (2019) employed the same methodology. The case with $A_B = 1$ corresponds to the original AGN feedback model by Harnois-Déraps et al. (2015), whereas $A_B = 0$ corresponds to the case of no effect of the baryon physics. Our treatment of baryon feedback effects in our cosmological analyses is described in Section 5.2.2.

4.2 Intrinsic alignment model

The so-called intrinsic alignment (IA) of galaxy shapes is another major astrophysical systematic in the measurement of the cosmic shear TPCFs (see Kirk et al. 2015; Troxel & Ishak 2015, for recent reviews). The IA comes both from the correlation between intrinsic shapes of two physically associated galaxies in the same local field (referred to as the II-term) and from the cross correlation between lensing shear of background galaxies and the intrinsic shape of foreground galaxies (referred to as the GI-term). We employ the standard theoretical model for these terms, namely, the nonlinear modification of the tidal alignment model (Hirata & Seljak 2004; Bridle & King 2007; Joachimi et al. 2011). In this formalism, TPCFs are given in a similar manner as the cosmic shear TPCFs, equations (8), (9), and (10), but with modified power spectra

$$\xi_{\text{II/GI}, \pm}^{ab}(\theta) = \frac{1}{2\pi} \int d\ell \ell J_{0,4}(\ell\theta) P_{\text{II/GI}}^{ab}(\ell), \quad (11)$$

with

$$P_{\text{II}}^{ab}(\ell) = \int_0^{\chi_H} d\chi F^2(\chi) \frac{p^a(\chi)p^b(\chi)}{f_K^2(\chi)} P_m^{NL} \left(\frac{\ell}{f_K(\chi)}, \chi \right), \quad (12)$$

$$P_{\text{GI}}^{ab}(\ell) = \int_0^{\chi_H} d\chi F(\chi) \frac{q^a(\chi)p^b(\chi) + p^a(\chi)q^b(\chi)}{f_K^2(\chi)} \times P_m^{NL} \left(\frac{\ell}{f_K(\chi)}, \chi \right). \quad (13)$$

In the above expressions, $F(\chi)$ represents the correlation strength between the tidal field and the galaxy shapes, for

which we adopt the same redshift dependent model as used in Hikage et al. (2019)

$$F[\chi(z)] = -A_{\text{IA}} C_1 \rho_{\text{crit}} \frac{\Omega_m}{D_+(z)} \left(\frac{1+z}{1+z_0} \right)^{\eta_{\text{eff}}}, \quad (14)$$

where A_{IA} is the amplitude parameter, C_1 is the fixed normalization constant ($C_1 = 5 \times 10^{-14} h^{-2} M_{\odot}^{-1} \text{Mpc}^3$), ρ_{crit} is the critical density at $z = 0$, and $D_+(z)$ is the linear growth factor normalized to unity at $z = 0$. We adopt the pivot redshift of $z_0 = 0.62$, and treat A_{IA} and the redshift dependence index η_{eff} as nuisance parameters in our cosmological analysis (see Section 5.2.2).

4.3 Corrections for the redshift-dependent selection bias, PSF related errors, and the constant shear

The theoretical model for the observed cosmic shear TPCFs is the sum of three components

$$\xi_{\pm}^{ab}(\theta) = \xi_{\text{GG},\pm}^{ab}(\theta) + \xi_{\text{GI},\pm}^{ab}(\theta) + \xi_{\text{II},\pm}^{ab}(\theta). \quad (15)$$

In reality, the measured TPCFs are affected by the redshift-dependent shear calibration bias (Section 2.3.1) and the residual PSF and PSF modeling error (Section 3.2, equation 7). In addition, ξ_+ components may be biased by the constant shear over a field arising from systematics (Appendix 1). We note that the constant shear arising from the gravitational lensing effect on scales larger than a survey field is taken into account properly in our analysis, as our model for the covariance matrix includes the super-survey mode. We apply these corrections to ξ_+ as

$$\begin{aligned} \xi_+^{ab}(\theta) \rightarrow & (1 + m_{\text{sel}}^a + m_R^a)(1 + m_{\text{sel}}^b + m_R^b) \xi_+^{ab}(\theta) \\ & + \alpha_{\text{psf}}^2 \xi_+^{pp}(\theta) + 2\alpha_{\text{psf}} \beta_{\text{psf}} \xi_+^{pq}(\theta) + \beta_{\text{psf}}^2 \xi_+^{qq}(\theta) \\ & + \bar{\gamma}^2, \end{aligned} \quad (16)$$

where $\bar{\gamma}$ is the redshift-independent constant shear term that we treat as a nuisance parameter (see Section 5.2.3). Since the PSF-related corrections to ξ_- are found to be very small (see Appendix 2), we do not apply these corrections to ξ_- . As a result, the corrected expression for ξ_- is

$$\xi_-^{ab}(\theta) \rightarrow (1 + m_{\text{sel}}^a + m_R^a)(1 + m_{\text{sel}}^b + m_R^b) \xi_-^{ab}(\theta). \quad (17)$$

The values of $(m_{\text{sel}}^a + m_R^a)$ are taken from Table 3 of Hikage et al. (2019); from the lowest to highest redshift bins, they are 0.0086, 0.0099, 0.0241, and 0.0391⁴. In our cosmological analysis, we treat α_{psf} and β_{psf} as nuisance parameters (see Section 5.2.3 for our choice of prior ranges).

⁴ While deriving the covariance, we also account for m_R in the mocks, although not the selection bias. This can cause an at most 2 percent difference in the covariance matrix.

4.4 Covariance

We derive a covariance matrix of the TPCF measurement using 2268 realizations of mock HSC shape catalogs. See Appendix 4 for a brief description of the mock catalogs, which are described in detail in Shirasaki et al. (2019). We measure the cosmic shear TPCFs for all 2268 mock catalogs in exactly the same manner as the real cosmic shear measurement. Since the HSC mock catalogs are constructed based on full-sky lensing simulation data with galaxy positions, intrinsic shape noise, and measurement noise taken from the real HSC shape catalog, the mock data naturally have the same survey geometry and the same noise properties as the real catalog, and include super-survey cosmic shear signal from these full-sky lensing simulations. In addition, the effects of nonlinear structure formation on the lensing shear field are included in the mock data. Therefore the covariance matrix computed from the mock catalogs automatically includes all the contributions, namely, Gaussian, non-Gaussian, super-survey covariance and the survey geometry are naturally taken into account. Shirasaki et al. (2019) found that in the case of the HSC 1st-year data we adopt in this study, the shape noise covariance dominates the covariance at the smallest angular bin, while the cosmological Gaussian covariance is prominent at the largest angular bin.

The accuracy of the covariance matrix from the mocks was studied in detail by Shirasaki et al. (2019). They investigated the impact of photo- z errors and field-to-field variation among the six separate HSC fields on the covariance estimation. They found that the change in the variance due to the different photo- z methods can yield a 5 – 10% difference in signal-to-noise ratio of the cosmic shear TPCFs, whereas the field variation can change the covariance estimation by 3 – 5%. Shirasaki et al. (2019) also addressed the effect of the multiplicative bias on the covariance estimation. They found that multiplicative bias of 10% can change shape noise covariance at the $\sim 20\%$ level. We already included the effect by assuming the fiducial value of multiplicative bias. A 1% level uncertainty in the multiplicative bias was confirmed in Mandelbaum et al. (2018b), leading to less than 2% uncertainty in our estimation of shape noise covariance.

Overall, we expect the covariance matrix estimated from mocks to be calibrated with $< 10\%$ accuracy against various systematic effects in the cosmic shear analysis, if the cosmological model in the mock catalogs is correct.

One drawback of this approach is that we are not able to include the cosmology dependence of the covariance, because the HSC mock catalogs are based on a set of full-sky gravitational lensing ray-tracing simulations that adopt a

specific flat Λ CDM cosmology (see Appendix 4). This is in contrast to Hikage et al. (2019) who used a halo-model-based analytic model of covariance matrix (which was tested against the HSC mock catalogs) in their cosmological analysis. In the case of the TPCF, the halo-model-based analytic covariance matrix was formulated (Cooray & Hu 2001; Takada & Jain 2009; Takada & Hu 2013). However, it is found in Shirasaki et al. (2019) that in order to derive an accurate covariance, the survey geometry must be properly taken into account which requires N_g^2 operations (N_g is a total number of galaxies) and is computationally very expensive. Hikage et al. (2019) also studied the effect of the cosmology dependence of the covariance on the cosmological analysis in their cosmic shear power spectrum study, by comparing cosmological constraints derived using the cosmology-dependent covariance (which is their fiducial model) with those derived using a cosmology-independent one (fixed to the best-fit cosmological model). They found that the best-fit Ω_m and $S_8 (= \sigma_8(\Omega_m/0.3)^\alpha)$ with $\alpha = 0.45$ or 0.5 values agree with each other within 20% of the statistical uncertainty. It is therefore reasonable to assume that the cosmology dependence of the covariance matrix does not significantly impact our cosmological analysis. We refer the readers to Eifler et al. (2009); Harnois-Déraps et al. (2019); Kodwani et al. (2019) for dependence of the covariance on cosmology and its impact on cosmological parameter constraints.

5 Cosmological analyses

We employ the standard Bayesian likelihood analysis for the cosmological inference of measured cosmic shear TPCFs. The log-likelihood is given by

$$-2\ln\mathcal{L}(\mathbf{p}) = \sum_{i,j} (d_i - m_i(\mathbf{p})) \text{Cov}_{ij}^{-1} (d_j - m_j(\mathbf{p})), \quad (18)$$

where d_i is the data vector that is detailed in Section 5.1, $m_i(\mathbf{p})$ is the theoretical model with \mathbf{p} is a set of parameters detailed in Section 5.2, and Cov_{ij} is the covariance matrix that is described in Section 4.4. Since our covariance matrix is constructed from 2268 mock realizations, its inverse covariance is known to be biased high (see Anderson 2003; Hartlap et al. 2007, and references therein). When calculating the inverse covariance, we therefore include the so-called Anderson-Hartlap correction factor $\alpha = (N_{\text{mock}} - N_d - 2)/(N_{\text{mock}} - 1)$, where $N_{\text{mock}} = 2268$ is the number of mock realizations (see Appendix 4) and $N_d = 170$ (for our fiducial choice, see Section 5.1) is the length of our data vector.

In order to sample the likelihood efficiently, we employ the multimodal nested sampling algorithm (Feroz &

Hobson 2008; Feroz et al. 2009, 2013), as implemented in the public software `MultiNest` (version 3.11).

5.1 Data vector

The data vector, d_i , is constructed from ten tomographic combinations of cosmic shear TPCFs $\hat{\xi}_+^{ab}$ and $\hat{\xi}_-^{ab}$ presented in Figure 2. Although TPCFs are detected with a good signal-to-noise ratio over a wide angular range as shown in the Figure, we limit angular ranges for our cosmological analysis for the following reasons.

First, we remove the angular range where the uncertainty in the theoretical model of cosmic shear TPCFs due to baryon physics is not negligible. We employ the AGN feedback model considered in Harnois-Déraps et al. (2015) as an extreme case, and deduce from Figure 5 of their paper that scales where the AGN feedback effect becomes less than 5% for ξ_+ and ξ_- are $\theta > 4'$ and $\theta > 20'$, respectively. Since their results were obtained assuming the galaxy redshift distribution with the mean redshift of $\langle z \rangle \sim 0.75$, the feedback effect may have a larger impact on larger scale signals for the lower source redshift sample. Considering the lower mean redshift of our lowest- z tomographic sample, we conservatively adopt about 50% larger scales than the scales mentioned above as our threshold scales.

Second, we remove the angular range where the extra shape correlations due to PSF leakage and PSF model error are not negligible. The effects of these errors on cosmic shear TPCFs are examined in Appendix 2. It is found that their total contribution to ξ_+ is about 10^{-6} on scales $5' < \theta < 60'$. Since this estimate is based on a simple model for PSF errors and the associated errors are large, $(0.4 - 1) \times 10^{-6}$, the above value should be considered as a rough estimate. Comparing this estimate with the measured signals and errors, we set an upper limit of $\theta \lesssim 60'$ for ξ_+ . Since the contribution of this systematic to ξ_- is found to be very small, about 10^{-8} even at around 1 degree scale, no upper limit is set to ξ_- from this condition.

Third, we remove the angular range where the signal-to-noise ratio including the cosmic variance for individual angular bins becomes $\lesssim 1$. This condition sets the upper limit $\theta \lesssim 200'$ for ξ_- .

Taking these three points into consideration, we adopt angular bins $\theta_i = 10^{0.1 \times i}$ arcmin with $9 \leq i \leq 17$ for ξ_+ , and $15 \leq i \leq 22$ for ξ_- . The corresponding angular ranges of galaxy-pair separation are $7'.08 < \theta < 56'.2$ and $28'.2 < \theta < 178'$ for ξ_+ and ξ_- , respectively. The total length of the data vector for our fiducial choice is $N_d = (9+8) \times 10 = 170$.

5.1.1 Signal-to-noise ratio

Using the fiducial data vector described in Section 5.1 and the covariance matrix described in Section 4.4, the total signal-to-noise ratio is found to be 18.7. The value of the signal-to-noise ratio depends on the assumed cosmological model through the covariance matrix. Our covariance matrix is based on the mock catalogs assuming *WMAP9* cosmology. Hikage et al. (2019) evaluated the total signal-to-noise of HSC tomographic cosmic shear power spectra using a covariance matrix based on the *Planck* cosmology, and found $SN = 15.6$ for their fiducial multipole range $300 < \ell < 1900$. The difference between these signal-to-noise ratio values is mostly accounted for by the different angular ranges adopted in these two studies (see also Appendix 5), and by the different cosmological models assumed for the covariance matrices.

5.1.2 Effective angular scale of angular bins and bin-averaged TPCFs

We determine the pair-weighted effective mean center of each angular bin as follows. In our TPCF measurements, we adopt a regular log-interval binning with the bin width of $\Delta \log \theta = 0.1$. For i -th bin, the minimum and maximum angular scales are given by $\theta_{min} = 10^{0.1(i-0.5)}$ and $\theta_{max} = 10^{0.1(i+0.5)}$, respectively, with the simple bin center of $\theta_c = 10^{0.1i}$. Assuming the number of galaxy pairs scales with separation as $n_p(\theta) \propto \theta^2$ (here we ignore the irregular survey geometry), the pair-number weighted mean separation for each bin is given by

$$\bar{\theta} = \frac{\int_{\theta_{min}}^{\theta_{max}} d\theta \theta n_p(\theta)}{\int_{\theta_{min}}^{\theta_{max}} d\theta n_p(\theta)}. \quad (19)$$

For our bin width of $\Delta \log \theta = 0.1$, we find $\bar{\theta} = 1.015 \times \theta_c$. We take this weighted mean separation as the effective angular scale of bins.

The same bin-averaged effect should be taken into account in the computation of the theoretical model of the cosmic shear TPCFs. The exact integration over the bin-width would be computationally expensive. Instead, we adopt an approximate estimate based on the following consideration (for other approximate estimates, see Asgari et al. 2019 and references therein). Assuming a power-law form for the cosmic shear TPCF within a bin-width, that is, $\xi(\theta) \propto \theta^\mu$ ($-1 \lesssim \mu \lesssim -0.5$ for the cosmic shear TPCFs on scales of our interest) and ignoring the irregular survey geometry, the bin-averaged TPCF is given by

$$\bar{\xi} = \frac{\int_{\theta_{min}}^{\theta_{max}} d\theta \xi(\theta) n_p(\theta)}{\int_{\theta_{min}}^{\theta_{max}} d\theta n_p(\theta)}. \quad (20)$$

In the case of $\mu = -1(-0.5)$, we find $\bar{\xi} = 0.989(0.994) \times \xi(\theta_c)$, which is very close to the value evaluated at the

effective angular scale of bins ($\bar{\theta}$). Specifically, $\xi(\bar{\theta}) = \xi(\theta_c) \times (\bar{\theta}/\theta_c)^\mu = 0.985(0.993) \times \xi(\theta_c)$, for $\mu = -1(-0.5)$. On these grounds, we decide to adopt the TPCFs at $\bar{\theta}$ as our estimate of the bin-averaged cosmic shear TPCFs.

5.2 Model parameters and prior ranges

In this subsection, we summarize model parameters and their prior ranges used in our cosmological analysis. Prior ranges and choice of parameter set for systematic tests are summarized in Table 1.

5.2.1 Cosmological parameters

We focus on the flat Λ CDM cosmological model characterized by six parameters (Ω_c , A_s , Ω_b , n_s , h , and $\sum m_\nu$, see Section 4.1). Among these parameters, the cosmic shear TPCFs are most sensitive to Ω_c and A_s , or the derived parameter σ_8 . Thus we adopt prior ranges that are sufficiently wide for these parameters (see Table 1). For (Ω_b , n_s , and h), which are only weakly constrained with cosmic shear TPCFs, we set prior ranges which largely bracket allowed values from external experiments (see Table 1). For the sum of neutrino mass, we take $\sum m_\nu = 0.06$ eV from the lower bound indicated by the neutrino oscillation experiments (e.g., Lesgourgues et al. 2013, for a review) for our fiducial choice. As a systematic test, we check the impact of neutrino mass on our conclusions by varying $\sum m_\nu$.

In addition to the fiducial Λ CDM model, we consider an extended model by including the time-independent equation-of-state parameter for the dark energy (w), referred to as the w CDM model. We take a flat prior with $-2 < w < -1/3$, which excludes the non-accelerating expansion of the present day Universe, and brackets allowed values from external experiments.

5.2.2 Astrophysical nuisance parameters

Our fiducial model for the TPCFs includes the contribution of the intrinsic alignment of galaxy shapes as described in Section 4.2. The nonlinear alignment model we employed has two parameters, the amplitude parameter A_{IA} and the redshift dependence parameter η_{IA} which represents the effective redshift evolution of the IA amplitude beyond the redshift evolution of the matter distribution due to a possible intrinsic redshift evolution and/or the change of the galaxy population as a function of redshift. Following recent cosmic shear studies e.g., Hildebrandt et al. (2017), Troxel et al. (2018), and Hikage et al. (2019), we adopt very wide prior ranges for these parameters.

The effect of baryon physics on the nonlinear matter power spectrum (see Section 4.1.1) is another possible as-

Table 1. Summary of cosmological, astrophysical, and systematics parameters used in our cosmological analysis. “flat[x_1, x_2]” means a flat prior between x_1 and x_2 , whereas “Gauss(\bar{x}, σ)” means a Gaussian prior with the mean \bar{x} and the standard deviation σ . For detail descriptions of parameters, see section 5.2.1 for the cosmological parameters, section 5.2.2 for the astrophysical nuisance parameters, and section 5.2.3 for the systematics nuisance parameters.

Parameter	Prior range		Systematics tests	Section
	Fiducial Λ CDM	w CDM		
Cosmological				5.2.1
Ω_c	flat[0.01, 0.9]			
$\log(A_s \times 10^9)$	flat[-1.5, 2.0]			
Ω_b	flat[0.038, 0.053]			
n_s	flat[0.87, 1.07]			
h	flat[0.64, 0.82]			
$\sum m_\nu$ [eV]	fixed to 0.06		flat[0, 0.5] for “ $\sum m_\nu$ varied”	
w	fixed to -1	flat[-2, -1/3]		
Astrophysical				5.2.2
A_{IA}	flat[-5, 5]		fixed to 0 for “w/o IA”	
η_{IA}	flat[-5, 5]		fixed to 3 for “IA $\eta_{IA} = 3$ ”	
A_B	fixed to 0		fixed to 1 for “ $A_B = 1$ ” or flat[-5, 5] for “ A_B varied”	
Systematics				5.2.3
α_{psf}	Gauss(0.029, 0.010)		fixed to 0 for “w/o PSF error”	
β_{psf}	Gauss(-1.42, 1.11)		fixed to 0 for “w/o PSF error”	
Δm	Gauss(0, 0.01)		fixed to 0 for “w/o Δm ”	
Δz_1	Gauss(0, 0.0374)		fixed to 0 for “w/o $p(z)$ error”	
Δz_2	Gauss(0, 0.0124)		fixed to 0 for “w/o $p(z)$ error”	
Δz_3	Gauss(0, 0.0326)		fixed to 0 for “w/o $p(z)$ error”	
Δz_4	Gauss(0, 0.0343)		fixed to 0 for “w/o $p(z)$ error”	
$\bar{\gamma}$	fixed to 0		flat[0, 5×10^{-3}] for “w/ const- γ ”	

trophysical systematic effect on the cosmological analysis. Nevertheless, since we restrict the angular ranges of cosmic shear TPCFs conservatively so that the baryon effects do not have a significant impact on our analysis (see Section 5.1), we do not include the baryon effect in our fiducial model, but check its impact in our systematics tests, employing the AGN feedback model by Harnois-Déraps et al. (2015) by adding a parameter A_B which controls the amplitude of the baryon effect. We carry out two tests; one fixing $A_B = 1$ that corresponds to the original AGN feedback model, and the other in which A_B is a free parameter.

5.2.3 Systematics nuisance parameters

To summarize, in our fiducial model we account for systematic effects from PSF leakage and PSF modeling errors, the uncertainty in the shear multiplicative bias correction, and uncertainties in the source galaxy redshift distributions. In our cosmological analysis, we include these effects by modeling them with nuisance parameters which are marginalized over in the final cosmological inference. In addition, in systematics tests we check the impact of the uncertainty of the constant shear over fields. Below we summarize our choices for prior ranges on nuisance parameters in these models.

Our models for the PSF leakage and PSF modeling errors are described in Section 3.2. We apply the correction for these systematics by equation (16). The model parameters are estimated in Appendix 2, in which we find $\alpha_{\text{psf}} = 0.029 \pm 0.010$ and $\beta_{\text{psf}} = -1.42 \pm 1.11$. We adopt Gaussian priors for these parameters and include them in our fiducial model.

Regarding the uncertainty in the shear multiplicative bias correction, we follow Hikage et al. (2019) to introduce the nuisance parameter Δm , which represents the residual multiplicative bias, and modifies the *theoretical prediction* for the cosmic shear TPCFs to

$$\xi_{\pm}^{ab}(\theta) \rightarrow (1 + \Delta m)^2 \xi_{\pm}^{ab}(\theta). \quad (21)$$

The prior range of Δm is taken to be Gaussian with zero mean and the standard deviation of 0.01. This is based on the calibration of the HSC first-year shear catalog done with image simulations (Mandelbaum et al. 2018b), in which it is confirmed that the multiplicative bias is controlled at the 1% level, leaving a 1% uncertainty on the residual bias.

Regarding uncertainties in the redshift distributions of source galaxies, we again follow the methodology of Hikage et al. (2019) (see also Troxel et al. 2018), in which uncertainties for each tomographic bin are assumed to be rep-

resented by a single parameter Δz_a . The source redshift distribution, which is derived by the COSMOS re-weighted method (see Section 2.2.1), is then shifted by

$$p^a(z) \rightarrow p^a(z + \Delta z_a). \quad (22)$$

The prior ranges for the shift parameters are estimated by comparing the COSMOS re-weighted $p^a(z)$ with ones derived from stacked-PDFs following the method described in Section 5.8 of Hikage et al. (2019). The derived prior ranges, which are summarized in Table 1, are in reasonable agreement with those found in Hikage et al. (2019) with the largest difference of 24%.

Finally, as discussed in Appendix 1, we introduce the single parameter $\bar{\gamma}$, which represents the redshift-independent constant shear arising from systematics, when checking the impact of the uncertainty in the constant shear over fields. The constant shear is added to the theoretical model of ξ_+ as shown in equation (16). Given that we have not found a strong evidence of the existence of the residual constant shear (see Appendix 1), we do not include it in our fiducial model, but check its impact as a systematics test, in which we treat $\hat{\gamma}$ as a nuisance parameter with a flat prior for a wide range $0 < \hat{\gamma} < 5 \times 10^{-3}$. We constrain $\hat{\gamma}$ to be positive, because only the square of $\hat{\gamma}$ enters ξ_+ .

5.2.4 Effective number of free parameters

It should be noted that not all the model parameters should be considered to be free as more than half of them are tightly constrained by priors. In other words, posteriors of those parameters are not driven by data but are dominated by priors, and fixing those parameters does not significantly change the cosmological constraints. In fact, as will be found in the following sections, although the total number of model parameters is 14 for our fiducial case (5 cosmological, 2 astrophysical, and 7 systematics parameters, see Table 1), only three of them (Ω_c , A_s , and A_{IA}) are constrained by the data with much narrower posterior distributions than with priors. Therefore, the standard definition of degree-of-freedom (d.o.f.) $N_d - N_p (= 170 - 14$ for our fiducial case) is likely to be an underestimation. A conservative choice of the effective number of free parameters (N_p^{eff}) should account for only these three parameters⁵.

⁵ See Raveri & Hu (2019) and Section 6.1 of Hikage et al. (2019) for a more mathematically robust way to define the effective number of free parameters.

6 Results

In this section we first present cosmological constraints from our cosmic shear analysis. We then discuss the robustness of the results against various systematics, and finally we perform internal consistency checks among different choices of angular ranges and of tomographic redshift bins.

6.1 Cosmological constraints in the fiducial flat Λ CDM model

First we compare the HSC tomographic cosmic shear TPCFs with the theoretical model with best-fit parameter values for the fiducial flat Λ CDM model in Figure 2, in which the measured ξ_+ are corrected for the PSF leakage and PSF modeling errors with equation (7). In these plots, error bars represent the square-root of the diagonal elements of the covariance matrix. We find that our model with the fiducial parameter setup reproduces the observed tomographic cosmic shear TPCFs quite well. The χ^2 value for the best-fit parameter set is $\chi^2 = 162.3$ for the *effective* d.o.f. of $170 - 3 = 167$, resulting in a p -value of 0.588.

We marginalize over a total of 14 model parameters (5 cosmological, 2 astrophysical, and 7 systematics parameters, see Table 1) in our fiducial flat Λ CDM model to derive marginalized posterior contours in the Ω_m - σ_8 and Ω_m - S_8 planes, which are presented in Figure 3. We also show marginalized one-dimensional posterior distributions of cosmological parameters in Figure 4. We find marginalized 68% confidence intervals of $0.247 < \Omega_m < 0.398$, $0.668 < \sigma_8 < 0.875$, and $0.775 < S_8 < 0.837$. From the posterior distributions shown in Figure 4, it can be seen that the current HSC cosmic shear TPCFs alone cannot place useful constraints on the Hubble constant (H_0), the baryon density parameter (Ω_b), and the spectral index (n_s). We have confirmed that the constraint on S_8 is not strongly affected by uncertainties in these parameters as long as they are restricted within the prior ranges considered in this paper.

6.1.1 Neutrino mass

Since the non-zero neutrino mass leads to a redshift-dependent suppression of the matter power spectrum at small scales, it has, in principle, an impact on the cosmological inference. In our fiducial setup, the neutrino mass is fixed at $\sum m_\nu = 0.06$ eV; the current measurement precision of the cosmic shear TPCFs is expected to be insufficient to place a useful constraint on the neutrino mass, especially given the fact that we exclude small scales from our analysis. We check this expectation with a setup in which the neutrino mass is allowed to vary with a flat

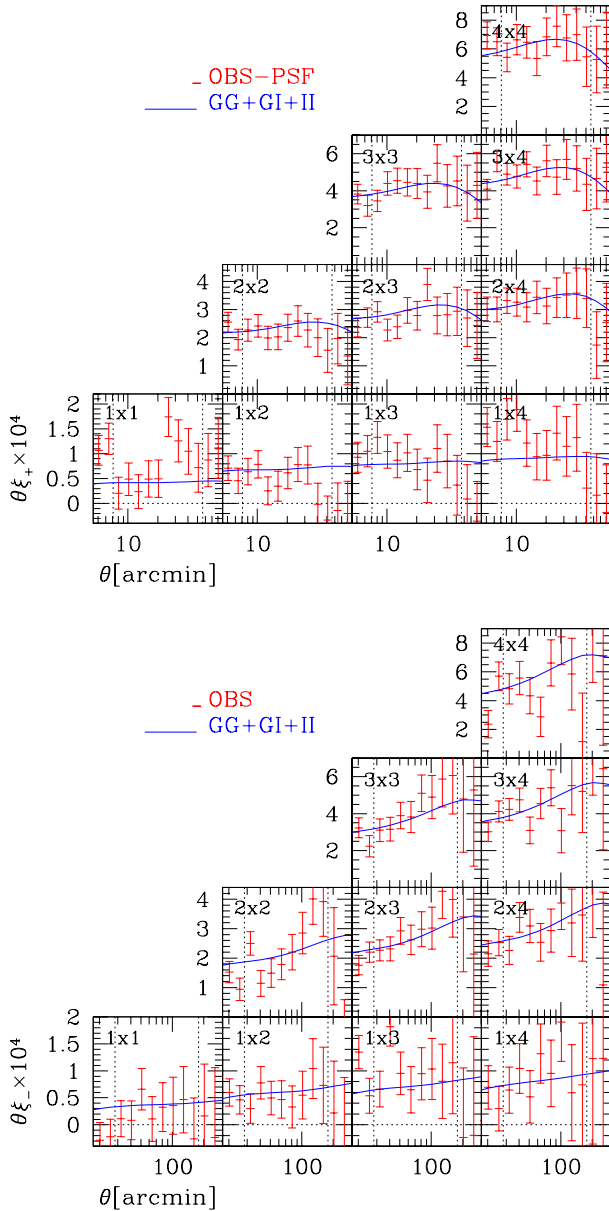


Fig. 2. Comparison of the HSC tomographic cosmic shear TPCFs with the best-fitting theoretical model for the fiducial flat Λ CDM model. Upper and lower triangular-tiled panels show ξ_+ and ξ_- , respectively. The measured ξ_+ are corrected for the PSF leakage and PSF modeling errors. Error bars represent the square-root of the diagonal elements of the covariance matrix. The solid line corresponds to the best-fit (maximum likelihood) fiducial model including the residual multiplicative bias correction shown in equation (21). Vertical dotted lines show the angular ranges used for the likelihood analysis.

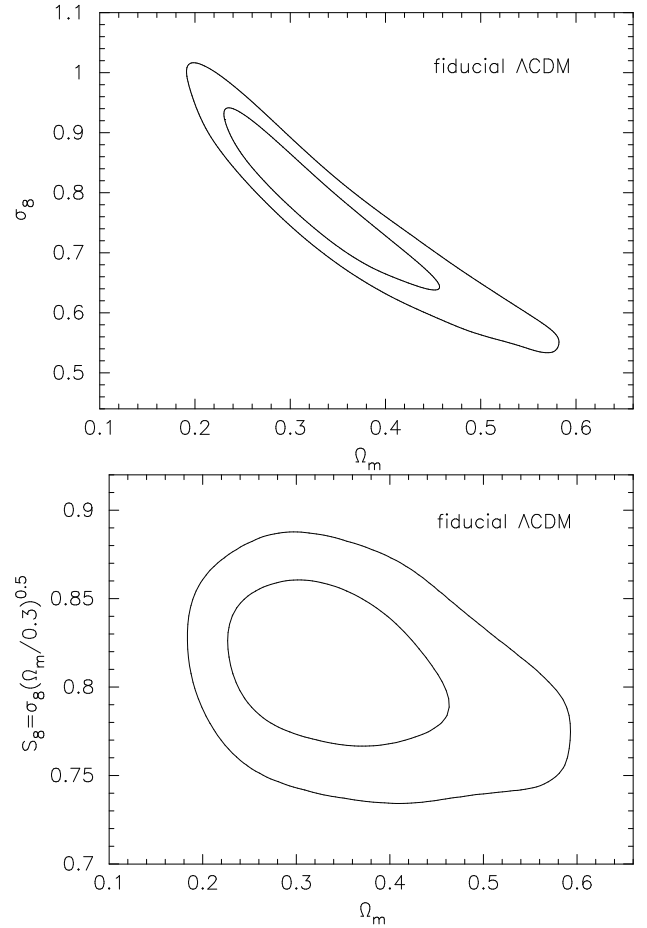


Fig. 3. Marginalized posterior contours (68% and 95% confidence levels) in the Ω_m - σ_8 plane (top panel) and in the Ω_m - S_8 plane (bottom panel), where $S_8 = \sigma_8 \sqrt{\Omega_m/0.3}$ in the fiducial flat Λ CDM model.

prior in the range $0 < \sum m_\nu < 0.5$ eV. Figure 5 shows the one-dimensional posterior distribution of $\sum m_\nu$, from which it is indeed found that the current HSC cosmic shear TPCFs do not place a useful constraint on the neutrino mass. The derived marginalized posterior contours in the Ω_m - σ_8 plane are compared with the fiducial case in panel (e) of Figure 6⁶. Confidence intervals on S_8 , Ω_m , and σ_8 are compared with the fiducial case in Figures 7, 8, and 9, respectively. These comparisons indicate that the non-zero neutrino mass indeed has little impact on our cosmological constraints. It is also found that the neutrino mass constraint does not correlate with any of Ω_m , σ_8 , or S_8 . These findings confirm the validity of our treatment of the neutrino mass in our fiducial cosmological inference.

⁶ At first look it may seem strange that the 68 percent confidence contours corresponding to the posterior distribution marginalized over neutrino masses is smaller than the case where we assume a fixed mass for neutrinos equal to 0.06 eV. This happens because the probability distribution is peaked at a value for $\sum m_\nu > 0.06$ eV where the posterior volume in Ω_m - σ_8 plane is smaller.

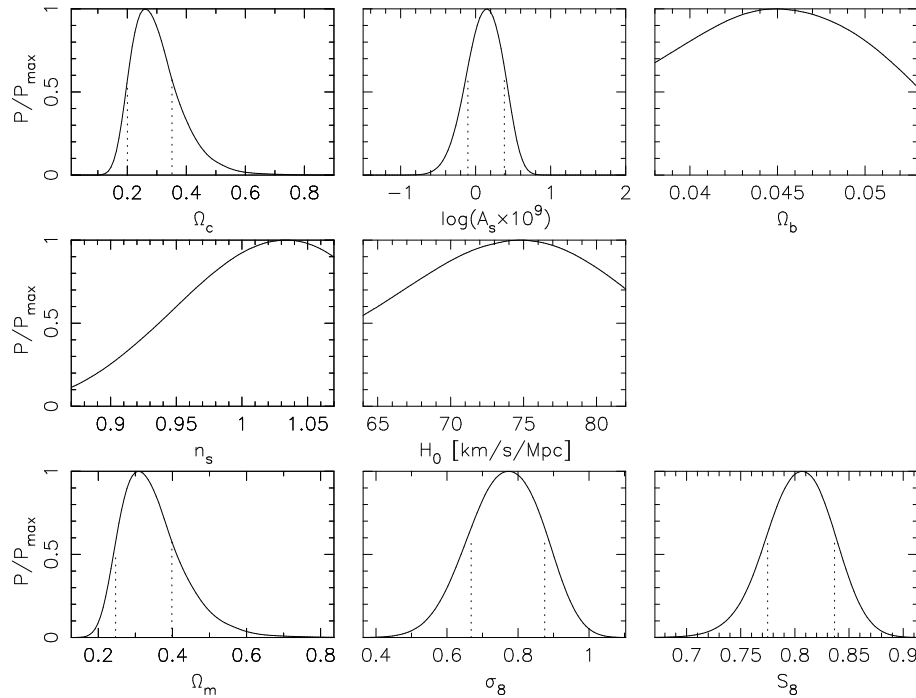


Fig. 4. Marginalized one-dimensional posterior distributions of different cosmological parameters in the fiducial flat Λ CDM model. The upper five panels show the posterior distributions for the model parameters, whereas the bottom three panels are for derived parameters. For the five top panels, the plotted range of the horizontal-axis indicates its flat prior range. Dotted vertical lines represent the approximate 68% confidence intervals, which are not shown for poorly constrained parameters.

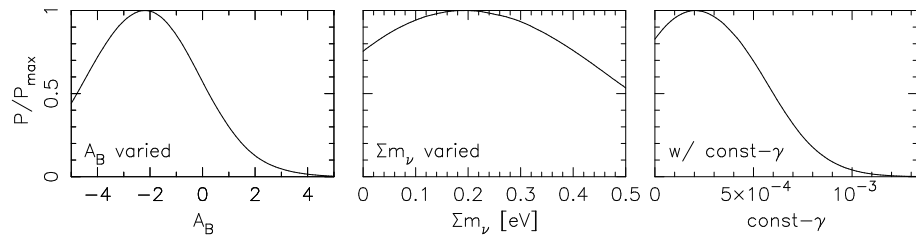


Fig. 5. Marginalized one-dimensional posterior distributions of nuisance parameters derived from non-fiducial models. From left to right, we show the baryon feedback model parameter from the “ A_B varied” setup, the neutrino mass from the “ Σm_ν varied” setup, and the residual constant shear $\bar{\gamma}$ from the “w/const- γ ” setup.

6.1.2 Posteriors of nuisance parameters

The marginalized one-dimensional posterior distributions of astrophysical and systematics parameters in the fiducial flat Λ CDM model are shown in Figure 10. It is found that, except for A_{IA} , the posteriors are dominated by priors. Below, we discuss effects of these nuisance parameters on the cosmological inference by changing the parameter setup. Comparisons of the one-dimensional constraints on S_8 , Ω_m , and σ_8 between the fiducial case and cases with different setups are summarized in Figures 7, 8, and 9, respectively.

6.2 Impact of astrophysical uncertainties

6.2.1 Intrinsic galaxy alignment

We find that the marginalized one-dimensional constraint on A_{IA} is $A_{IA} = 0.91^{+0.27}_{-0.32}$, which is consistent with the result from the HSC cosmic shear power spectrum analysis by Hikage et al. (2019). They found $A_{IA} = 0.38 \pm 0.70$ for their fiducial setup. The 1σ error on A_{IA} from our analysis is smaller than one from the power spectrum analysis. The reason for this is currently not known. A possible reason would be different angular ranges adopted in the two analyses (see Appendix 5). On the other hand, our constraint on η_{IA} is -2.5 ± 2 , which is consistent with the shear power spectrum analysis. As discussed in section 5.4 of Hikage et al. (2019), a plausible value of η_{IA} from available observations is $\eta_{IA} = 3 \pm 0.75$ which would be about

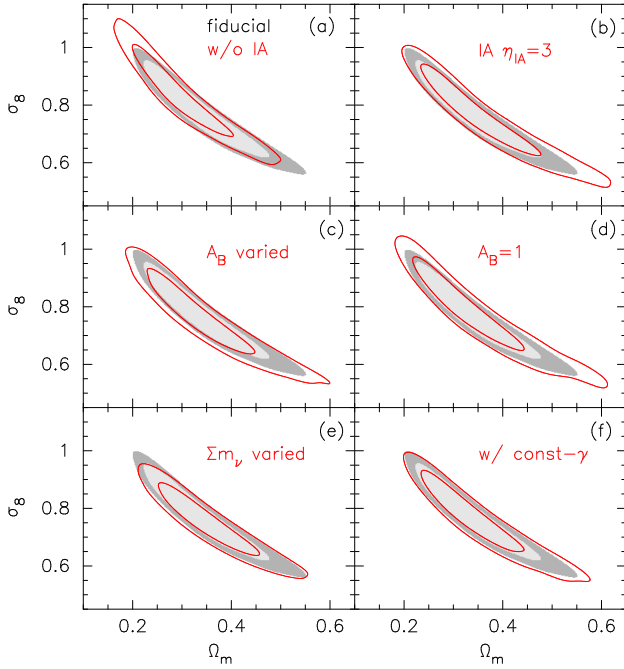


Fig. 6. Comparison of constraints in the Ω_m - σ_8 plane between the fiducial setup (gray contours) and different assumptions, as described in the text (red contours showing 68% and 95% confidence levels).

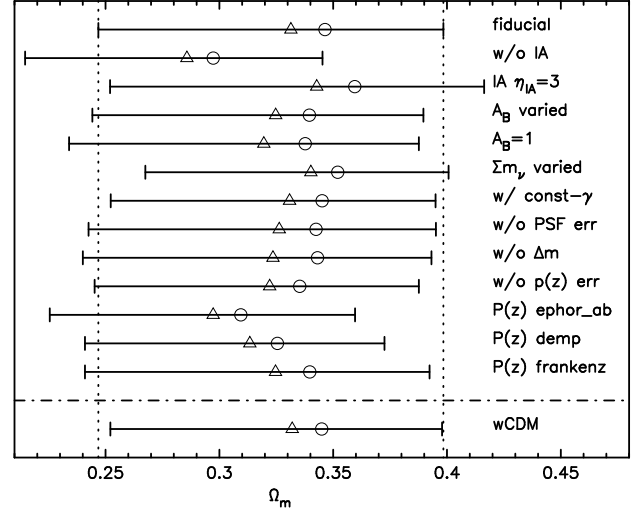


Fig. 8. Same as Fig 7, but for marginalized one-dimensional constraints on Ω_m . Open circles and open triangles show the means and medians of the marginalized posterior distributions, respectively. We note that the means of the marginalized posterior distributions are preferentially located on the right side of the 68% confidence intervals, because their posterior distributions are skewed toward high Ω_m values (as shown in Figure 4).

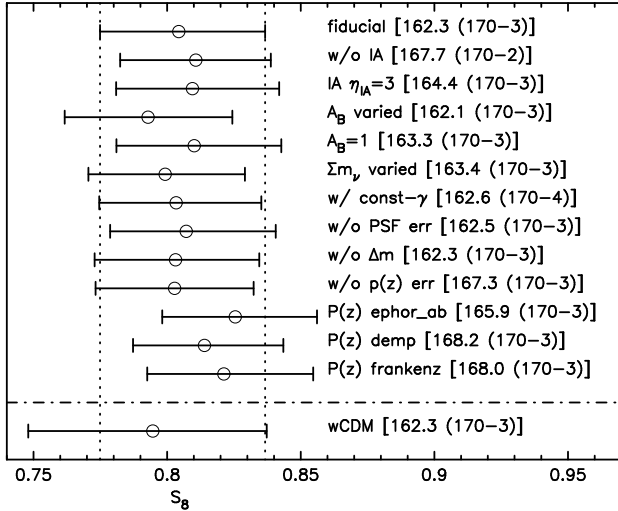


Fig. 7. Means and 68% confidence intervals of marginalized one-dimensional constraints on $S_8 = \sigma_8 \sqrt{\Omega_m}/0.3$. The fiducial case (top) is compared with different setups to check the robustness of our result. Vertical dotted lines show the 68% confidence interval of the fiducial case. The numbers in the bracket after the setup name indicate $[\chi_{\min}^2 (N_d - N_p^{\text{eff}})]$.

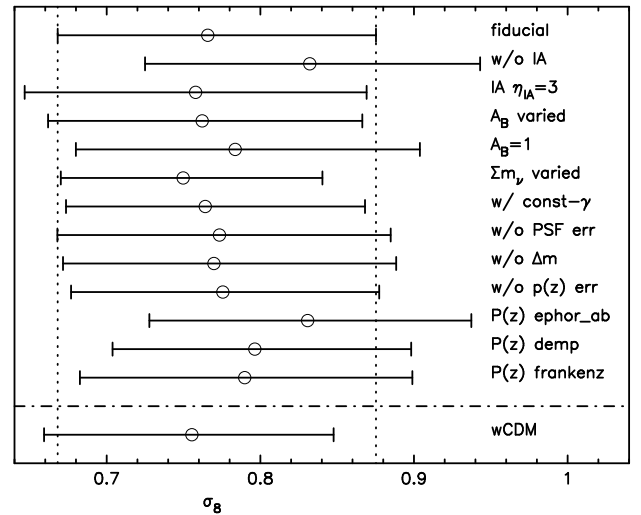


Fig. 9. Same as Fig 7, but for marginalized one-dimensional constraints on σ_8 .

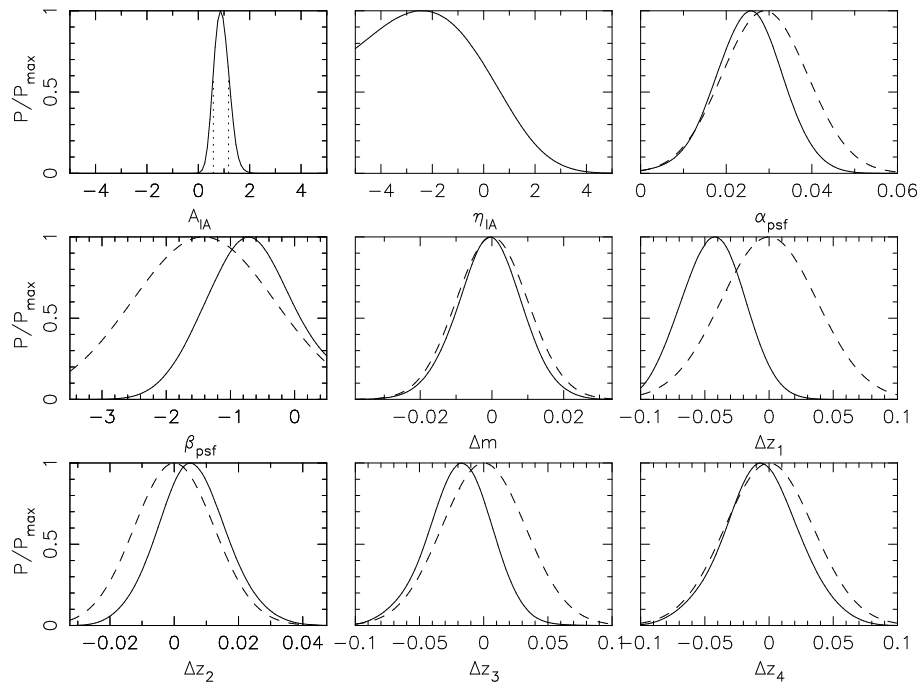


Fig. 10. Marginalized one-dimensional posterior distributions of astrophysical and systematics parameters in the fiducial flat Λ CDM model. For the cases of A_{IA} and η_{IA} , the horizontal axis range corresponds to the flat prior range ($-5 < x < 5$), whereas for the other cases Gaussian priors are shown by the dashed curves. In the top left panel, vertical lines represent the approximate 68% confidence interval of A_{IA} .

2σ higher compared to our derived value. Given this, we will examine the impact of the IA modeling on our cosmological inference below.

In order to test the robustness of the cosmological constraints against the uncertainty of the intrinsic galaxy alignment, we perform two cosmological inferences with different IA modeling. In one case, the IA contribution is completely ignored i.e., A_{IA} is fixed to 0, and in the other case η_{IA} is fixed to 3 (See section 5.4 of Hikage et al. 2019) while A_{IA} is treated as a free parameter. The results from these settings are compared with the fiducial ones in Figure 6 (panels (a) and (b)) and Figure 7. We find that the corresponding changes in cosmological constraints are not significant. For instance, the shift of the mean S_8 value is found to be 0.16σ for the “IA $\eta_{\text{IA}} = 3$ ” case.

Finally, we examine how the IA contribution affects the constraints in the Ω_m - σ_8 plane. As shown in panel (a) of Figure 6, the inclusion of the IA contribution moves the posterior contour toward higher Ω_m and lower σ_8 , and as we have seen, slightly reduces S_8 . This behavior may appear somewhat counter-intuitive, because the IA contribution, mostly given a negative GI term, suppresses TPCFs, leading to a larger S_8 to compensate. A plausible explanation for this is as follows. Since the negative redshift dependence of IA contribution, which is preferred as seen in Figure 10, suppresses TPCFs at lower redshifts more strongly than at higher redshifts, larger matter fluctuations

at lower redshifts are required to compensate the redshift-dependent suppression. This requires more rapid growth of matter fluctuations at lower redshifts, leading to the higher Ω_m along with the lower σ_8 to adjust the overall amplitude of tomographic TPCFs.

6.2.2 Baryonic feedback

In our fiducial setup, we do not include the effect of the baryonic feedback, but instead remove the angular scales where its impact is not negligible (see Section 5.1). It is therefore expected that the baryonic feedback effect does not strongly affect our cosmological constraints. We check this expectation explicitly by employing an empirical “AGN feedback model” by Harnois-Déraps et al. (2015) (as described in Section 4.1.1). Specifically we consider two cases; the original AGN feedback model by Harnois-Déraps et al. (2015), which corresponds to fixing the baryon feedback parameter $A_B = 1$, and a more flexible model in which A_B is allowed to vary with a flat prior in the range $-5 < A_B < 5$.

Since the baryonic feedback suppresses the amplitude of the matter power spectrum on scales we are probing, it leads to a higher values of S_8 to compensate. This is indeed seen in the “ $A_B = 1$ ” case, as shown in Figure 7. However the shift of the mean S_8 value is not significant, 0.1σ , as expected.

In the “ A_B varied” case, Figure 5 shows that the con-

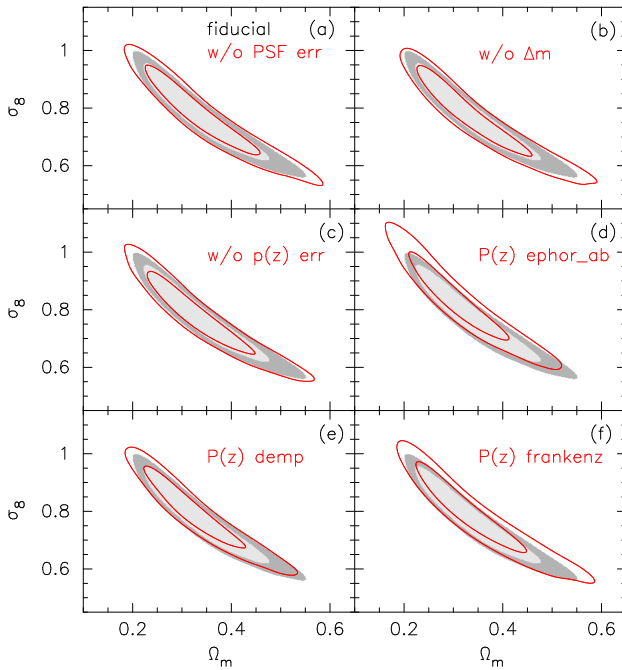


Fig. 11. Same as Figure 6, but for other setups for systematics tests.

straint on A_B is very weak with the marginalized posterior of (its mean and σ) $A_B = -1.8 \pm 1.8$. The expected correlation between A_B and S_8 is confirmed. Again, it is found from panel (c) of Figure 6 and Figure 7 that its impact on cosmological constraints is not significant. We conclude that the effect of baryonic feedback on our fiducial cosmological constraints is insignificant given the size of our statistical errors.

6.3 Impact of systematics

6.3.1 Residual constant shear

In the fiducial model, we do not include the correction for the residual constant shear, because the statistical significance of its existence is found to be marginal (see Appendix 1). In order to check the robustness of our fiducial cosmological constraints against the residual constant shear, we test the same setup as the fiducial case but including a single parameter $\bar{\gamma}$ that models the residual constant shear as equation (16). We adopt a flat prior in the range $0 < \bar{\gamma} < 5 \times 10^{-3}$. The derived constraints are compared with the fiducial case in panel (f) of Figure 6 and Figure 7. We find that the resulting changes in the cosmological constraints are very small. The marginalized one-dimensional posterior distribution of $\bar{\gamma}$ is shown in Fig 5. The derived 1σ upper limit is found to 4.4×10^{-4} , which is smaller than the constant shear expected from the cosmic shear that is coherent over the field (see Appendix 4.1).

6.3.2 PSF leakage and PSF modeling errors

In this paper we employ a simple model for the PSF leakage and PSF modeling errors given by equation (6), and apply the correction to the cosmic shear TPCFs as described in equation (16). The priors for the model parameters α_{psf} and β_{psf} are derived in Appendix 2. Marginalized one-dimensional posterior distributions of these parameters from our fiducial analysis are shown in Figure 10. We found that the posteriors are largely determined by the priors. We also find that the marginalized constraints on these parameters are not strongly correlated with either Ω_m , σ_8 , or S_8 .

In order to check the robustness of our cosmological constraints against these systematics, we test the same setup as the fiducial case but ignoring these parameters i.e., setting $\alpha_{\text{psf}} = \beta_{\text{psf}} = 0$. The results are shown in panel (a) of Figure 11 and Figure 7. We find that the changes in the cosmological constraints are very small. This is expected, as the corrections due to PSF leakage and PSF modeling errors small compared with the current size of errors on the HSC cosmic shear TPCFs.

6.3.3 Shear calibration error

In our fiducial analysis we also take account of the uncertainty in the shear multiplicative bias correction using a simple model, equation (21), with a Gaussian prior corresponding to a 1% uncertainty (see Section 5.2.3). The marginalized one-dimensional posterior distribution of the model parameter Δm from our fiducial analysis is shown in Figure 10, which indicates that the posterior is dominated by the prior.

In order to check the effect of this residual calibration bias on our cosmological constraints, we test the same setup as the fiducial case but ignoring the nuisance parameter i.e., setting $\Delta m = 0$. The results are shown in panel (b) of Figure 11 and Figure 7. We find that the changes in the cosmological constraints are very small.

6.3.4 Source redshift distribution errors

We take account of uncertainties in the redshift distributions of source galaxies by introducing parameters Δz_a , which represent a shift of the source redshift distributions as defined in equation (22). We consider independent shifts for the four tomographic bins, leading to four nuisance parameters. Priors on these parameters are determined based on differences of source redshift distributions from different approaches (see Section 5.2.3), and we marginalize over these nuisance parameters in our fiducial setup. Marginalized one-dimensional posterior distributions of these parameters from our fiducial analysis are shown in Figure 10. Although peak positions of these

posteriors show shifts from the peak the prior distributions, the sizes of the shifts are reasonably within the the Gaussian priors. In the case of the lowest redshift bin which shows the largest shift, the peak shift is 1.1σ of the Gaussian priors, and thus is not statistically significant. However, notice that it may indicate an unknown bias in estimation of the source redshift distribution that is not captured in the prior knowledge.

In order to check the robustness of our cosmological constraints against these uncertainties, we test the same setup as the fiducial analysis but ignoring these parameters. The results are shown in panel (c) of Figure 11 and Figure 7. We find that the changes in the cosmological constraints are small, with the shift of the mean S_8 value being -0.05σ .

In addition, we also check for possible systematic effects coming from the uncertainty of the redshift distributions due to photo- z methodology. We explore this by replacing the default COSMOS re-weighted $p^a(z)$ with ones derived from stacked PDFs. For this purpose we adopt three different photo- z methods, DEmp, Ephor AB, and FRANKEN-Z (see Section 2.2.1), for which stacked PDFs are shown in Figure 1. This is a rather empirical test, as each photo- z method has its own bias and errors (Tanaka et al. 2018), thus this test should be considered as a sensitivity check. The results are shown in Figure 11 (panels (d), (e), and (f)) and Figure 7. Again, we find that the changes in the cosmological constraints are not significant. Thus we conclude that no additional systematics are identified from this test.

6.4 Internal consistency

Here we present results of internal consistency checks in which we derive cosmological constraints from subsets of the data vector and compare the results with ones from a reference setup. In doing so, we do not use the fiducial results as the reference, but instead we adopt the results from the “cosmology alone” setup in which we include neither systematics nor astrophysical parameters but only five cosmological parameters are included as a baseline for comparison. The reason for this choice is to avoid undesirable changes in nuisance parameters, especially redshift-dependent parameters such as the redshift dependence parameter of the IA η_{IA} and photo- z error parameters Δz_i , which may add or cancel out shifts in parameter constraints. Of course, this has the side effect that the reference setup does not provide the best cosmological constraints, although the difference from the fiducial case is not significant. In fact, the differences in the marginalized cosmological constraints between the fiducial setup

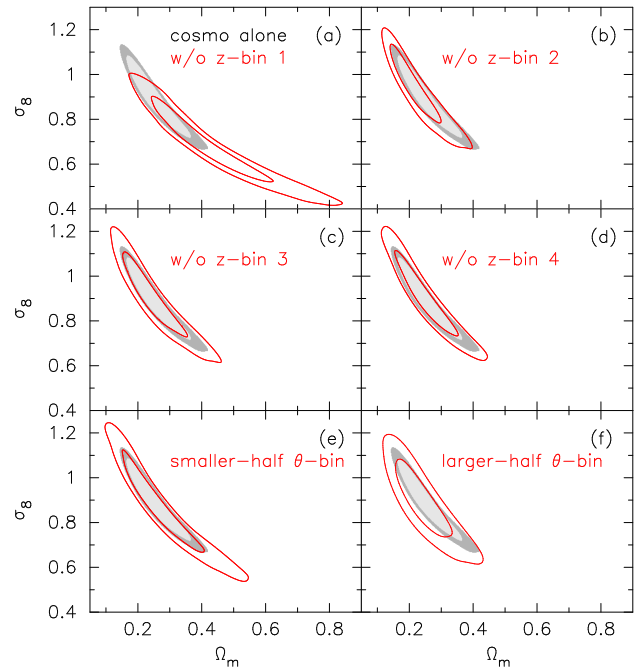


Fig. 12. Comparison of constraints in the Ω_m - σ_8 plane from the cosmology alone setup (gray contours) with different setups for internal consistency checks (red contours showing 68% and 95% confidence levels).

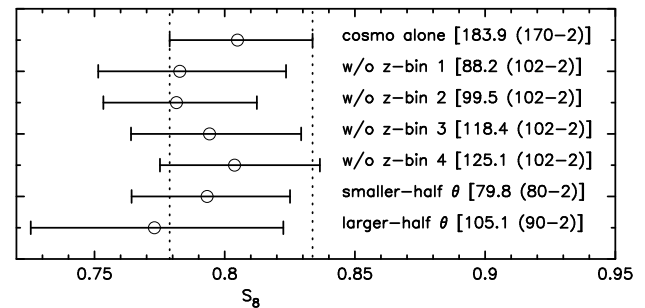


Fig. 13. Means and 68% confidence intervals of marginalized one-dimensional constraints on S_8 . The “cosmology alone” case (top) is compared with different setups for internal consistency checks. Vertical dotted lines show the 68% confidence interval of the cosmology alone case.

and “cosmology alone” setup is about the level of these between the fiducial setup and “w/o IA” setup, as ignoring IA contribution has the largest effect. To summarize, considering the facts that our aim here is to carry out an *internal* consistency check and that the side effect is not significant, we adopt “cosmology alone” setup as the reference.

6.4.1 Tomographic redshift bins

First, we exclude one of the four redshift bins and perform the cosmological inference with three tomographic bins. The resulting cosmological constraints are shown in Figure 12 (panels (a)-(d)), and the derived 68% confidence intervals of S_8 are compared in Figure 13. We find that

constraints on S_8 from these setups are consistent within 1σ of the reference result. Figure 13 may look odd in the sense that all the setups have a lower mean value of S_8 than that of the reference setup. This is a result of changes of the posterior distributions in the Ω_m - σ_8 plane in different directions, leading to a smaller S_8 by chance. Also Figure 12 shows that 68% confidence contours in the Ω_m - σ_8 plane in these cases largely overlap with the reference contour. Thus we conclude that no significant internal inconsistency is found from this test.

It may be worth noting that excluding one redshift bin leads to relatively large shifts in Ω_m constraints, as shown in Figure 12. This is due to the fact that the constraint on Ω_m is mainly driven by the relative amplitudes of cosmic shear TPCFs in different tomographic bins, as was discussed in Hikage et al. (2019).

6.4.2 Angular ranges

Next, we check the internal consistency among different angular ranges by splitting the fiducial angular bins in half. To be specific, the 9(8) angular bins of ξ_+ (ξ_-) are split into 4(4) smaller θ bins and 5(4) larger θ bins. The resulting cosmological constraints, in comparison with the ‘‘cosmology alone’’ case, are shown in Figure 12 (panels (e) and (f)) and Figure 13. It is found that for the smaller-half bins case, the constraint on S_8 shifts to smaller value by 0.42σ , with the posterior contours on Ω_m - σ_8 plane being elongated along the Ω_m - σ_8 degeneracy direction. On the other hand, the constraint on S_8 from the larger-half bins case shifts slightly more than 1σ of the reference result. However, the 68% confidence interval of this case is about two times larger than that of the reference case. In addition, the confidence contours in the Ω_m - σ_8 plane largely overlap with those of reference cases. Thus no strong evidence of internal inconsistency is found by this test.

6.5 w CDM model

In addition to the fiducial Λ CDM model, we test one extension model by including the time-independent dark energy equation of state parameter w . We allow w to vary with a flat prior in the range $-2 < w < -1/3$. The setup of the other parameters are same as the fiducial Λ CDM model.

The marginalized constraints in the Ω_m - σ_8 , Ω_m - w , and S_8 - w planes are shown in Figure 14, along with constraints from the fiducial Λ CDM model and the *Planck* 2018 results for the w CDM model (Planck Collaboration et al. 2018, TT+TE+EE+lowE). Marginalized one-dimensional constraint ranges of Ω_m , σ_8 , and S_8 are shown in Figures 8, 9, and 7, respectively. It is found that adding w as a model parameter degrades constraints on cosmological parame-

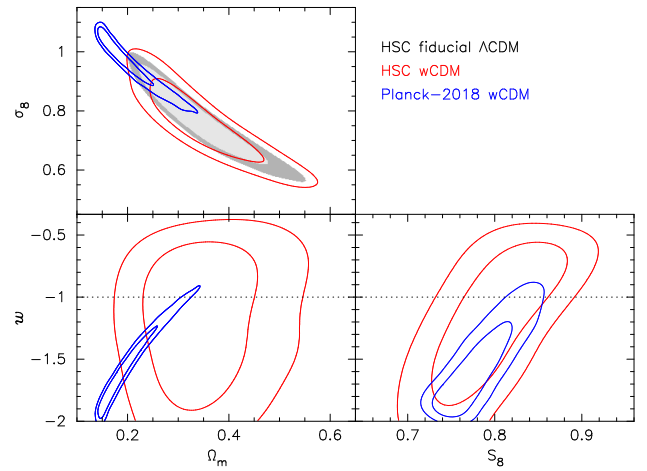


Fig. 14. Marginalized posterior contours (68% and 95% confidence levels) in the Ω_m - σ_8 plane (top), the Ω_m - w plane (bottom left) and the S_8 - w plane (bottom right) in the w CDM model are shown by red contours. Constraints from the fiducial Λ CDM model are shown by the gray contours, and *Planck* 2018 results for the w CDM model (Planck Collaboration et al. 2018, TT+TE+EE+lowE) are also shown by blue contours.

ters, and that the current HSC cosmic shear TPCFs alone cannot place a useful constraint on w . This is quantitatively very similar to the result found in the HSC cosmic shear power spectrum analysis by Hikage et al. (2019).

6.6 Comparison to other constraints from the literature

Finally, we compare the cosmological constraints from our fiducial Λ CDM model with other results in the literature. Comparison plots in the Ω_m - σ_8 plane are presented in Figure 15, where constraints from other studies are derived from publicly available chains. Note that although different studies adopt different priors, we do not adjust them to our fiducial setup, but rather use their original priors. Also, different studies adopt different modeling choices, for example, Dark Energy Survey Year 1 (DES-Y1; Troxel et al. 2018) adopts the uniform sampling of A_S , instead of the logarithmic sampling that adopted in KiDS+VIKING-450 (Hildebrandt et al. 2018) and this study. Therefore, part of the difference in the posteriors may be due to the different choices of priors and modeling. Figure 16 compares the 68% confidence intervals of $S_8 = \sigma_8 \sqrt{\Omega_m/0.3}$, where results of other studies are taken from the literature.

DES-Y1 covers much larger area (1321 deg^2) than the HSC first year data, yielding slightly tighter constraints than our fiducial results. The confidence contours of DES-Y1 in the Ω_m - σ_8 plane largely overlap with our results, although our confidence regions are roughly 1.3 times larger than theirs. However, the two constraints are slightly mis-

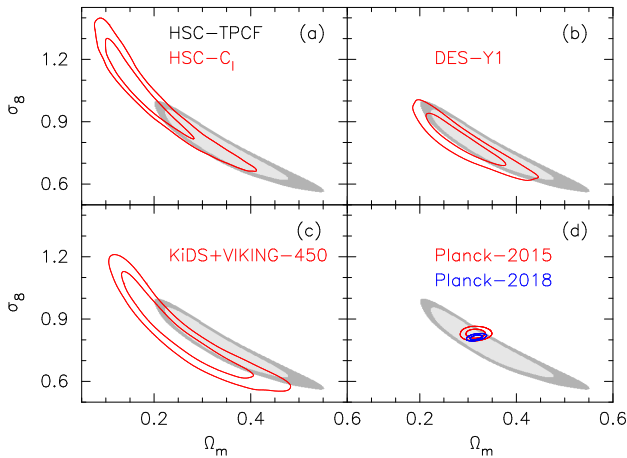


Fig. 15. Marginalized posterior contours (68% and 95% confidence levels) in the Ω_m - σ_8 plane. Our result from the fiducial Λ CDM model (gray contours) is compared with results in the literature (red-line contours): Note that although different studies adopt different priors and different modeling choices, we do not adjust them to our fiducial setup, but rather use their original setups. Therefore, part of the difference in the posteriors may be due to the different choice of priors and modeling. (A) HSC first-year cosmic shear power spectrum result (Hikage et al. 2019). (b) Dark Energy Survey Year 1 (DES-Y1) cosmic shear TPCF result (Troxel et al. 2018). (c) KiDS+VIKING-450 cosmic shear TPCF result (Hildebrandt et al. 2018). (d) *Planck* 2018 CMB result without CMB lensing (Planck Collaboration et al. 2018, TT+TE+EE+lowE) (red lines) and *Planck* 2015 CMB result without CMB lensing (Planck Collaboration et al. 2016, TT+lowP) (blue lines).

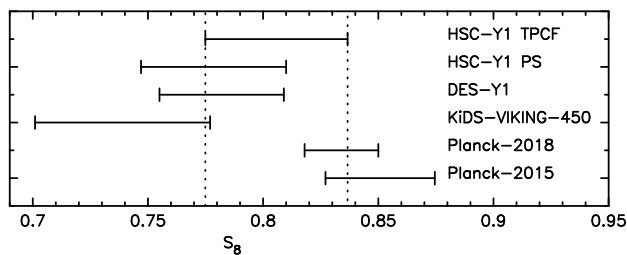


Fig. 16. 68% confidence intervals of marginalized posterior distributions of $S_8 = \sigma_8 \sqrt{\Omega_m/0.3}$. Our result from the fiducial Λ CDM model is compared with other results in the literature, HSC first year (HSC-Y1) cosmic shear power spectra (Hikage et al. 2019), DES-Y1 cosmic shear TPCFs (Troxel et al. 2018), KiDS+VIKING-450 cosmic shear TPCFs (Hildebrandt et al. 2018), and *Planck* 2018 CMB (? , TT+TE+EE+lowE), and *Planck* 2015 CMB (Planck Collaboration et al. 2016, TT+lowP without lensing). Since different studies adopt different definitions of the central values (mean, median, or peak of the posterior distribution), central values are not shown to avoid possible misunderstanding.

aligned in the direction perpendicular to the Ω_m - σ_8 degeneracy direction. This results in about 1σ difference in best-fit S_8 values, as seen in Figure 16.

KiDS+VIKING-450 covers 341.3 deg^2 . A large part of our survey fields are included in their survey fields. Their total number of galaxies is ~ 12 million, about 30% larger than our sample. The redshift range of galaxies they used in their cosmological analysis is $0.1 < z < 1.2$, which is lower than the redshift range adopted in our analysis, $0.3 < z < 1.5$. As is found in Figure 15, compared with our posterior contours, contours from KiDS+VIKING-450 are located on the lower Ω_m side, and are slightly elongated to the higher- σ_8 direction. Their best-fit S_8 value is about 2σ lower than ours, but our error bars overlap (see Fig. 16).

It is found from Figure 15 that the confidence contours in the Ω_m - σ_8 plane from the *Planck* 2018 CMB result (Planck Collaboration et al. 2018, TT+TE+EE+lowE without CMB lensing) as well as *Planck* 2015 CMB result (Planck Collaboration et al. 2018, TT+lowP without CMB lensing) overlap well with our confidence contours from the HSC first year TPCF analysis. The 68% confidence intervals of S_8 from *Planck* 2015 and 2018 are also consistent with our result, although S_8 from *Planck* prefers a slightly higher value than our constraints. We therefore conclude that there is no tension between *Planck* 2015 and 2018 constraints and our cosmic shear constraints. The concordance between our HSC cosmic shear TPCF result and the *Planck* CMB result in the flat Λ CDM model will place useful constraints on extended models such as the w CDM model, although a combined cosmological inference with *Planck* data is beyond the scope of this study. In fact, a comparison between those constraints shown in Figure 14 implies that a tighter lower limit on w may be obtained by such a combined analysis.

6.7 Comparison with HSC first year cosmic shear power spectrum result

Figure 15 indicates that the 68% confidence contours from the cosmic shear power spectrum analysis by Hikage et al. (2019) and from this study overlap only mildly, even though they share the same HSC first year weak lensing shape catalog (Mandelbaum et al. 2018a) and adopt a similar analysis setup, including the definition of tomographic bins and the treatment of the IA and systematics parameters. The 68% marginalized one-dimensional confidence intervals of Ω_m and σ_8 from these two studies also overlap only slightly. For instance, Figure 16 indicates that there is $\sim 1\sigma$ difference in the S_8 constraints between these two studies. The differences between the median values of S_8 and Ω_m are -0.024 and -0.17 , respectively, where

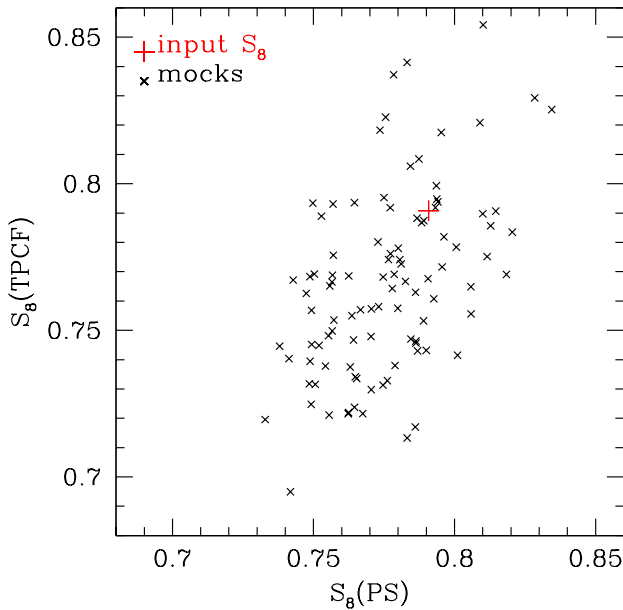


Fig. 17. Scatter plot showing median values of marginalized one-dimensional posterior distributions of S_8 derived from cosmological analyses on 100 mock catalogs. Results from the power spectrum analysis by Hikage et al. (2019) are compared with ones from the TPCF analysis in this study. The red cross shows the value of S_8 adopted in generating the mock catalogs.

the standard deviations of those parameters found in this study is 0.031 and 0.087, respectively. These differences could be indicative of unknown systematic errors in either or both of the analyses and/or originate from different angular scales used in those two cosmological analyses, and therefore we will examine this carefully below.

We use realistic HSC mock catalogs to check whether these differences can be explained simply by a statistical fluctuation. The mock catalogs used in this analysis are the ones described in Oguri et al. (2018) and adopted in Hikage et al. (2019). These differ slightly from the mock catalogs used in this paper to derive the covariance matrix in Appendix 4, although we note that these two sets of mock catalogs are generated by almost the same methodology and therefore are very similar. We perform the cosmological inference on the 100 mock catalogs using the same parameter setup as the fiducial setup except that we fix the PSF modeling errors α_{psf} and β_{psf} to zero because no PSF modeling error is added in the mock data. Hikage et al. (2019) also performed their power-spectrum based cosmological inference on the same mock catalogs adopting their fiducial setup. From these analyses on the mocks, we can determine the covariance of best-fit cosmological parameters between the cosmic shear power spectrum analysis in Hikage et al. (2019) and our cosmic shear TPCF analysis.

We present the scatter plot comparing S_8 values from

these two cosmological analyses on the same mock catalogs in Figure 17. We find that S_8 values from these two analyses are only weakly correlated. We find that the correlation is even weaker for Ω_m . We find that, for S_8 , 10 out of 100 cases have a difference ΔS_8 less than the observed value of -0.024 , and for Ω_m , 14 out of 100 cases have a difference $\Delta\Omega_m$ less than the observed difference of -0.17 . If we take the two-side estimate, we find that for $S_8(\Omega_m)$, 40(16) out of 100 cases have an absolute difference of $|\Delta S_8| > 0.024$ ($|\Delta\Omega_m| > 0.17$). These mean that these differences can be explained by a statistical fluctuation at the $\sim 1.4\sigma$ level.

To quantify the covariance of best-fit cosmological parameters further, we compute the correlation coefficient

$$r(q) = \frac{\text{Cov}(q_R, q_F)}{\text{Cov}(q_R, q_R)^{1/2} \text{Cov}(q_F, q_F)^{1/2}}, \quad (23)$$

where q is either S_8 or Ω_m , and the subscripts R and F stand for the real-space TPCF and Fourier-space power spectrum, respectively. We find $r(S_8) = 0.50$ and $r(\Omega_m) = 0.16$, which confirms that the correlation between derived cosmological constraints from the two analyses is weak, especially for Ω_m . The main reason for this weak correlation is the different multipole ranges probed in these two analyses. Hikage et al. (2019) adopted the multipole range $300 < \ell < 1900$, whereas in Appendix 5, we examine the contribution to ξ_{\pm} from different ℓ -ranges to show that a large part of the contribution to ξ_{\pm} on scales adopted in this study comes from $\ell < 300$. This indicates that in deriving cosmological constraints, these two studies utilize fairly different and complementary information.

7 Summary and conclusions

We have presented a cosmological analysis of the cosmic shear TPCFs measured from the HSC first year data, covering 136.9 deg^2 and including 9 million galaxies to $i \sim 24.5$ AB mag. We used the HSC first year shape catalog (Mandelbaum et al. 2018a), which is based on the re-Gaussianization PSF correction method (Hirata & Seljak 2003) and is calibrated with image simulations (Mandelbaum et al. 2018b). In order to examine the impact of residual PSF errors on cosmic shear TPCFs, we utilized the HSC star catalog which contains information on both the star shapes and PSF models. Photometric redshifts derived from the HSC five-band photometry are adopted to divide galaxies into four tomographic redshift bins ranging from $z = 0.3$ to 1.5 with equal widths of $\Delta z = 0.3$. The unweighted galaxy number densities for each tomographic bin are (from the lowest to highest redshift) $5.9, 5.9, 4.3,$ and 2.4 arcmin^{-2} .

In addition to the HSC data set, we utilized HSC mock shape catalogs constructed based on full-sky gravitational

lensing ray-tracing simulations (Takahashi et al. 2017). The mock catalogs have the same survey geometry and shape noise properties as the real data (Shirasaki et al. 2019). We derived the covariance matrix adopted in our cosmological analysis from 2268 mock realizations. The mock catalogs are also used to assess the statistical significance of some of our results.

Ten combinations of auto and cross tomographic TPCFs were measured with high signal-to-noise ratio over a wide angular range. The total signal-to-noise ratio computed over the angular ranges that we adopted in our cosmological analysis ($7' < \theta < 56'$ for ξ_+ and $28' < \theta < 178'$ for ξ_-) was $S/N = 18.7$, although a caveat is that this estimate depends on the cosmological model used to derive the covariance matrix; we adopt the WMAP9 cosmology. We also examined the E/B-mode decomposition of the cosmic shear TPCFs to test our assumption in the cosmological analysis that the cosmic shear field is B-mode free. In appendix 3, we evaluated the standard χ^2 value for B-mode TPCFs with the shape noise covariance, and found $\chi^2 = 86.9$ for $N_d = 90$. We thus conclude that no evidence of significant B-mode shear is found.

We performed a standard Bayesian likelihood analysis for the cosmological inference of the measured cosmic shear TPCFs. Our fiducial Λ CDM model consists of five cosmological parameters and includes contributions from intrinsic alignment of galaxies as well as seven nuisance parameters (2 for PSF errors, 1 for shear calibration error, and 4 for source redshift distribution errors). We found that our model fits the measured TPCFs very well with a minimum χ^2 of 162.3 for 167 effective degrees-of-freedom. Marginalized one-dimensional constraints are (mean and 68% confidence interval) $S_8 = \sigma_8 \sqrt{\Omega_m/0.3} = 0.804^{+0.032}_{-0.029}$, $\Omega_m = 0.346^{+0.052}_{-0.100}$, and $\sigma_8 = 0.766^{+0.110}_{-0.098}$. Although we fixed the neutrino mass of $\sum m_\nu = 0.06$ eV in the fiducial model, we found that varying the neutrino mass has little effect on the cosmological constraints. We also tested w CDM model to find that allowing the dark energy equation of state parameter w to vary degrades the S_8 constraint to $S_8 = 0.795^{+0.043}_{-0.047}$. We have found that the current HSC cosmic shear TPCFs alone cannot place a useful constraint on w .

We have carefully checked the robustness of our cosmological results against astrophysical uncertainties in modeling and systematics uncertainties in measurements. The former includes the intrinsic alignment of galaxies and the baryonic feedback effect on the nonlinear matter power spectrum, and the latter includes PSF errors, shear calibration error, errors in the estimation of source redshift distributions, and a residual constant shear over fields. We have tested the validity of our treatment of those uncer-

tainties by changing parameter setups or by adopting extreme models for them. We have found that none of these uncertainties has a significant impact on the cosmological constraints. Specifically, different setups yield shifts in best-fit S_8 values of $\sim 0.6\sigma$ of the statistical error at most. We have also confirmed the internal consistency of our results among different redshift and angular bins.

Our constraint contours in the Ω_m - σ_8 plane largely overlap with those of DES-Y1 (Troxel et al. 2018), although the two contours are slightly misaligned, resulting in about a 1σ difference in the best-fit S_8 value; our best-fit S_8 is higher than that from DES-Y1. A larger difference was found between KiDS+VIKING-450 (Hildebrandt et al. 2018) and our result. In fact, the best-fit S_8 value from KiDS+VIKING-450 is $\sim 2\sigma$ lower than our result. We have found that the S_8 constraint from *Planck* (Planck Collaboration et al. 2018) is consistent with our result within 1σ level. We found that the 68% confidence contour in the Ω_m - σ_8 plane from *Planck* nicely overlaps with our result.

Hikage et al. (2019) used the same HSC first year weak lensing shape catalog but adopted the cosmic shear power spectra to derive cosmological constraints. We have found about a 1σ level difference in S_8 constraints between the cosmic shear power spectrum analysis and our cosmic shear TPCF analysis, even though they share the same shape catalog. We used mock catalogs to examine the statistical significance of the difference. We have found that the difference can be explained by a statistical fluctuation at about the 1.4σ level. We also used the mock catalog to examine the correlation in derived cosmological constraints between these two studies, and have found the cross-correlation coefficients of $r(S_8) = 0.50$ and $r(\Omega_m) = 0.16$. The reason for these weak correlations, especially for Ω_m , is the different multipole ranges probed in these two analyses. Hikage et al. (2019) adopted the multipole range $300 < \ell < 1900$, whereas a large part of the contribution to ξ_\pm over angular ranges adopted in this study comes from $\ell < 300$, indicating that two studies utilize fairly different and complementary information in deriving cosmological constraints.

In summary, our S_8 constraint is located on the high side among recent cosmic shear studies and is fully consistent with the latest *Planck* CMB result. Among the recent studies mentioned above, only the KiDS+VIKING-450 result is inconsistent with our result at $\sim 2\sigma$ level. Since the KiDS survey fields largely overlap with HSC survey fields, it is worth analyzing their public shape catalog with our methodology to understand its origin, which we leave for future work.

This paper presents cosmological results based on the

HSC 1st-year data. When the HSC survey is completed, we will have about seven times more area, which will improve both the statistical error and the cosmic variance. In addition to this, improvement efforts on several analysis techniques are underway, including PSF measurement and modeling (Aihara et al. 2019), photo- z estimations, and shear measurements. In future, it would be important to explore other missing redshift-dependent selection biases by using techniques such as metacalibration (Huff & Mandelbaum 2017; Sheldon & Huff 2017), and it would be also important to implement more advanced methods of accounting for baryonic feedback effects such as one proposed by Eifler et al. (2015).

Recently, Joudaki et al. (2019) argued that the systematic uncertainties in the redshift distribution of galaxies derived by the re-weighted method bases on the COSMOS 30-band photo- z (Ilbert et al. 2009) might be underestimated and could lead to a bias in the cosmological constraints due to outliers in the COSMOS 30-band catalog. They showed that S_8 constraints from both KiDS-VIKING 450 and DES-Y1 inferred adopting the redshift distributions based on spectroscopic samples are lower than ones based on COSMOS 30-band photo- z sample. A plausible reason for these differences could be the systematic uncertainties in the COSMOS 30-band photo- z , though further close examination of the redshift distribution is needed to reach a firm conclusion. One might deduce from their finding that a similar bias may exist in our analysis. Take the case of DES-Y1 for example, the difference between S_8 values inferred adopting the two redshift distributions is $|\Delta S_8| = 0.030$ (Joudaki et al. 2019), which corresponds to $\sim 1\sigma$ of our S_8 constraint. Thus, this is indeed one important issue to be explored in a future study (see Appendix 6 for a related discussion). However, in our case it is not feasible to use spec- z samples for a reference sample, because a spec- z sample that reaches the depth of HSC weak lensing catalog is not available now. A possible method to calibrate the photo- z without relying on COSMOS 30-band photo- z is a cross-correlation method (Newman 2008) which we will adopt in a future work.

Acknowledgments

We would like to thank the anonymous referee for constructive comments on the earlier manuscript which improved the paper. We would like to thank R. Takahashi for useful discussions and for making full-sky gravitational lensing simulation data publicly available. We would like to thank Martin Kilbinger for making the software **Athena** publicly available, Antony Lewis and Anthony Challinor for making the software **CAMB** publicly available, **MultiNest** developers for **MultiNest** publicly available, and HEALPix team for HEALPix software publicly available.

This work was supported in part by World Premier International Research Center Initiative (WPI Initiative), MEXT, Japan, JSPS KAKENHI Grant Number JP15H05887, JP15H05892, JP15H05893, 17H06600, JP17K05457, 18H04350, 18H04358, and JP18K03693. A portion of this research was carried out at the Jet Propulsion Laboratory, California Institute of Technology, under a contract with the National Aeronautics and Space Administration. RMa is supported by the Department of Energy Cosmic Frontier program, grant DE-SC0010118.

Data analysis were in part carried out on PC cluster at Center for Computational Astrophysics, National Astronomical Observatory of Japan. Numerical computations were in part carried out on Cray XC30 and XC50 at Center for Computational Astrophysics, National Astronomical Observatory of Japan, and also on Cray XC40 at YITP in Kyoto University.

The Hyper Suprime-Cam (HSC) collaboration includes the astronomical communities of Japan and Taiwan, and Princeton University. The HSC instrumentation and software were developed by the National Astronomical Observatory of Japan (NAOJ), the Kavli Institute for the Physics and Mathematics of the Universe (Kavli IPMU), the University of Tokyo, the High Energy Accelerator Research Organization (KEK), the Academia Sinica Institute for Astronomy and Astrophysics in Taiwan (ASIAA), and Princeton University. Funding was contributed by the FIRST program from Japanese Cabinet Office, the Ministry of Education, Culture, Sports, Science and Technology (MEXT), the Japan Society for the Promotion of Science (JSPS), Japan Science and Technology Agency (JST), the Toray Science Foundation, NAOJ, Kavli IPMU, KEK, ASIAA, and Princeton University. This paper makes use of software developed for the Large Synoptic Survey Telescope. We thank the LSST Project for making their code available as free software at <http://dm.lsst.org>

The Pan-STARRS1 Surveys (PS1) have been made possible through contributions of the Institute for Astronomy, the University of Hawaii, the Pan-STARRS Project Office, the Max-Planck Society and its participating institutes, the Max Planck Institute for Astronomy, Heidelberg and the Max Planck Institute for Extraterrestrial Physics, Garching, The Johns Hopkins University, Durham University, the University of Edinburgh, Queen's University Belfast, the Harvard-Smithsonian Center for Astrophysics, the Las Cumbres Observatory Global Telescope Network Incorporated, the National Central University of Taiwan, the Space Telescope Science Institute, the National Aeronautics and Space Administration under Grant No. NNX08AR22G issued through the Planetary Science Division of the NASA Science Mission Directorate, the National Science Foundation under Grant No. AST-1238877, the University of Maryland, and Eotvos Lorand University (ELTE) and the Los Alamos National Laboratory.

Based in part on data collected at the Subaru Telescope and retrieved from the HSC data archive system, which is operated by Subaru Telescope and Astronomy Data Center at National Astronomical Observatory of Japan.

References

Aihara, H., Armstrong, R., Bickerton, S., et al. 2018a, PASJ,

- 70, S8
- Aihara, H., Arimoto, N., Armstrong, R., et al. 2018b, PASJ, 70, S4
- Aihara, H., AlSayyad, Y., Ando, M., et al. 2019, arXiv e-prints, arXiv:1905.12221
- Alam, S., Ata, M., Bailey, S., et al. 2017, MNRAS, 470, 2617
- Anderson, L., Aubourg, É., Bailey, S., et al. 2014, MNRAS, 441, 24
- Anderson, T. W. 2003, An introduction to multivariate statistical analysis, 3rd edn. (Wiley-Interscience)
- Asgari, M., Heymans, C., Hildebrandt, H., et al. 2019, A&A, 624, A134
- Bernstein, G. M., & Jarvis, M. 2002, AJ, 123, 583
- Betoule, M., Kessler, R., Guy, J., et al. 2014, A&A, 568, A22
- Bird, S., Viel, M., & Haehnelt, M. G. 2012, MNRAS, 420, 2551
- Bosch, J., Armstrong, R., Bickerton, S., et al. 2018, PASJ, 70, S5
- Bridle, S., & King, L. 2007, New Journal of Physics, 9, 444
- Challinor, A., & Lewis, A. 2011, Phys. Rev. D, 84, 043516
- Chang, C., Jarvis, M., Jain, B., et al. 2013, MNRAS, 434, 2121
- Chisari, N. E., Richardson, M. L. A., Devriendt, J., et al. 2018, MNRAS, 480, 3962
- Cooray, A., & Hu, W. 2001, ApJ, 554, 56
- Crittenden, R. G., Natarajan, P., Pen, U.-L., & Theuns, T. 2002, ApJ, 568, 20
- Dark Energy Survey Collaboration, Abbott, T., Abdalla, F. B., et al. 2016, MNRAS, 460, 1270
- de Jong, J. T. A., Verdoes Kleijn, G. A., Kuijken, K. H., & Valentijn, E. A. 2013, Experimental Astronomy, 35, 25
- Eifler, T., Krause, E., Dodelson, S., et al. 2015, MNRAS, 454, 2451
- Eifler, T., Schneider, P., & Hartlap, J. 2009, A&A, 502, 721
- Feroz, F., & Hobson, M. P. 2008, MNRAS, 384, 449
- Feroz, F., Hobson, M. P., & Bridges, M. 2009, MNRAS, 398, 1601
- Feroz, F., Hobson, M. P., Cameron, E., & Pettitt, A. N. 2013, ArXiv e-prints, arXiv:1306.2144
- Furusawa, H., Koike, M., Takata, T., et al. 2018, PASJ, 70, S3
- Górski, K. M., Hivon, E., Banday, A. J., et al. 2005, ApJ, 622, 759
- Harnois-Deraps, J., Giblin, B., & Joachimi, B. 2019, arXiv e-prints, arXiv:1905.06454
- Harnois-Déraps, J., van Waerbeke, L., Viola, M., & Heymans, C. 2015, MNRAS, 450, 1212
- Hartlap, J., Simon, P., & Schneider, P. 2007, A&A, 464, 399
- Hellwing, W. A., Schaller, M., Frenk, C. S., et al. 2016, MNRAS, 461, L11
- Hikage, C., Oguri, M., Hamana, T., et al. 2019, PASJ, 71, 43
- Hildebrandt, H., Viola, M., Heymans, C., et al. 2017, MNRAS, 465, 1454
- Hildebrandt, H., Köhlinger, F., van den Busch, J. L., et al. 2018, arXiv e-prints, arXiv:1812.06076
- Hinshaw, G., Larson, D., Komatsu, E., et al. 2013, ApJS, 208, 19
- Hirata, C., & Seljak, U. 2003, MNRAS, 343, 459
- Hirata, C. M., & Seljak, U. 2004, Phys. Rev. D, 70, 063526
- Hsieh, B. C., & Yee, H. K. C. 2014, ApJ, 792, 102
- Huff, E., & Mandelbaum, R. 2017, arXiv e-prints, arXiv:1702.02600
- Ilbert, O., Capak, P., Salvato, M., et al. 2009, ApJ, 690, 1236
- Jain, B., & Seljak, U. 1997, ApJ, 484, 560
- Jing, Y. P., Zhang, P., Lin, W. P., Gao, L., & Springel, V. 2006, ApJ, 640, L119
- Joachimi, B., Mandelbaum, R., Abdalla, F. B., & Bridle, S. L. 2011, A&A, 527, A26
- Joudaki, S., Hildebrandt, H., Traykova, D., et al. 2019, arXiv e-prints, arXiv:1906.09262
- Kaiser, N. 1992, ApJ, 388, 272
- Kaiser, N., Squires, G., & Broadhurst, T. 1995, ApJ, 449, 460
- Kawanomoto, S., Uruguchi, F., Komiyama, Y., et al. 2018, PASJ, 70, 66
- Kilbinger, M. 2015, Reports on Progress in Physics, 78, 086901
- Kirk, D., Brown, M. L., Hoekstra, H., et al. 2015, Space Sci. Rev., 193, 139
- Kodwani, D., Alonso, D., & Ferreira, P. 2019, The Open Journal of Astrophysics, 2, 3
- Köhlinger, F., Viola, M., Joachimi, B., et al. 2017, MNRAS, 471, 4412
- Komiyama, Y., Obuchi, Y., Nakaya, H., et al. 2018, PASJ, 70, S2
- Laigle, C., McCracken, H. J., Ilbert, O., et al. 2016, ApJS, 224, 24
- Lesgourgues, J., Mangano, G., Miele, G., & Pastor, S. 2013, Neutrino Cosmology
- Mandelbaum, R. 2018, ARA&A, 56, 393
- Mandelbaum, R., Miyatake, H., Hamana, T., et al. 2018a, PASJ, 70, S25
- Mandelbaum, R., Lanusse, F., Leauthaud, A., et al. 2018b, MNRAS, 481, 3170
- McCarthy, I. G., Schaye, J., Bird, S., & Le Brun, A. M. C. 2017, MNRAS, 465, 2936
- Mead, A. J., Peacock, J. A., Heymans, C., Joudaki, S., & Heavens, A. F. 2015, MNRAS, 454, 1958
- Miralda-Escude, J. 1991, ApJ, 380, 1
- Miyazaki, S., Komiyama, Y., Kawanomoto, S., et al. 2018, PASJ, 70, S1
- Newman, J. A. 2008, ApJ, 684, 88
- Oguri, M., Miyazaki, S., Hikage, C., et al. 2018, PASJ, 70, S26
- Osato, K., Shirasaki, M., & Yoshida, N. 2015, ApJ, 806, 186
- Planck Collaboration, Ade, P. A. R., Aghanim, N., et al. 2016, A&A, 594, A13
- Planck Collaboration, Aghanim, N., Akrami, Y., et al. 2018, ArXiv e-prints, arXiv:1807.06209
- Raveri, M., & Hu, W. 2019, Phys. Rev. D, 99, 043506
- Schaye, J., Dalla Vecchia, C., Booth, C. M., et al. 2010, MNRAS, 402, 1536
- Schneider, P., van Waerbeke, L., Kilbinger, M., & Mellier, Y. 2002, A&A, 396, 1
- Semboloni, E., Hoekstra, H., Schaye, J., van Daalen, M. P., & McCarthy, I. G. 2011, MNRAS, 417, 2020
- Sheldon, E. S., & Huff, E. M. 2017, ApJ, 841, 24
- Shirasaki, M., Hamana, T., Takada, M., Takahashi, R., & Miyatake, H. 2019, MNRAS, 486, 52
- Shirasaki, M., Takada, M., Miyatake, H., et al. 2017, MNRAS, 470, 3476

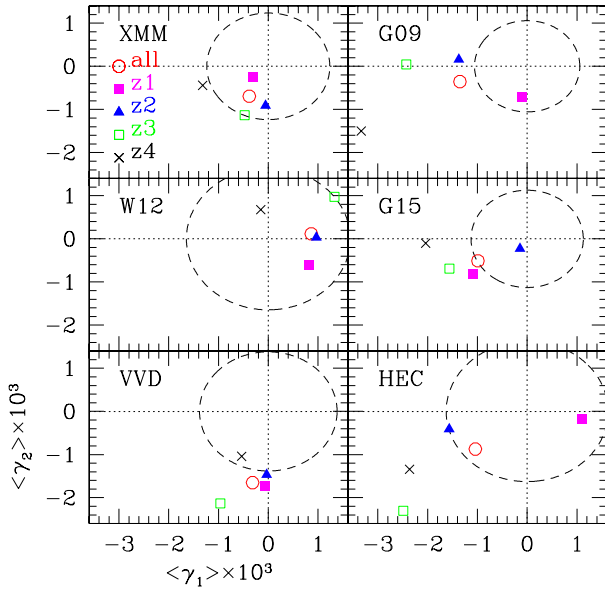


Fig. 18. Measured mean shear values over each field are plotted for each tomographic sample (magenta filled squares, blue triangles, green open squares, and black crosses from the lowest to highest redshift tomographic bins, respectively), and for the combined sample of all four tomographic bins (red open circles). The dashed circle shows the 68.3% enclosing mean cosmic shear value for the combined sample, as estimated from mock catalogs (see Appendix 1). The 68.3% enclosing mean shear values for each tomographic bin are about 0.77, 1.1, 1.4, and 1.7 times larger than those for the combined sample for the lowest to highest redshift tomographic bins, respectively.

- Shirasaki, M., & Yoshida, N. 2014, *ApJ*, 786, 43
- Smith, R. E., Peacock, J. A., Jenkins, A., et al. 2003, *MNRAS*, 341, 1311
- Springel, V., Pakmor, R., Pillepich, A., et al. 2018, *MNRAS*, 475, 676
- Suzuki, N., Rubin, D., Lidman, C., et al. 2012, *ApJ*, 746, 85
- Takada, M., & Hu, W. 2013, *Phys. Rev. D*, 87, 123504
- Takada, M., & Jain, B. 2009, *MNRAS*, 395, 2065
- Takahashi, R., Hamana, T., Shirasaki, M., et al. 2017, *ApJ*, 850, 24
- Takahashi, R., Sato, M., Nishimichi, T., Taruya, A., & Oguri, M. 2012, *ApJ*, 761, 152
- Tanaka, M., Coupon, J., Hsieh, B.-C., et al. 2018, *PASJ*, 70, S9
- Troxel, M. A., & Ishak, M. 2015, *Phys. Rep.*, 558, 1
- Troxel, M. A., MacCrann, N., Zuntz, J., et al. 2018, *Phys. Rev. D*, 98, 043528
- van Daalen, M. P., Schaye, J., Booth, C. M., & Dalla Vecchia, C. 2011, *MNRAS*, 415, 3649
- Weinberg, D. H., Mortonson, M. J., Eisenstein, D. J., et al. 2013, *Phys. Rep.*, 530, 87
- White, M. 2004, *Astroparticle Physics*, 22, 211
- Zhan, H., & Knox, L. 2004, *ApJ*, 616, L75

Table 2. Summary of χ^2 and p -values of the mean shear over each field, where there are 8 degrees of freedom (2 shear components multiplied by 4 tomographic bins), and the covariance matrix is derived from mock catalogs (see Appendix 4).

Field	χ^2	p -value
XMM	4.6	0.80
GAMA09H	17.2	0.028
WIDE12H	5.2	0.73
GAMA15H	13.7	0.089
VVDS	9.1	0.33
HECTOMAP	14.8	0.063

Appendix 1 Mean shear values over fields

The value of the shear averaged over a field is not expected to be zero due to the presence of the cosmic shear signal on scales larger than a field. However, it could also be non-zero due to residual systematics in the shear estimation and/or data reduction process. The latter, if present, may bias the cosmological inference. While systematic tests on the HSC 1st-year shape catalog (Mandelbaum et al. 2018a) found no evidence of a mean shear above that expected from large-scale cosmic shear, we closely reexamine this question here because the shear correlation function, especially ξ_+ , is directly affected by the residual mean shear.

The measured mean shear values over each field are shown in Figure 18 for each tomographic sample, as well as for the combined sample of the four tomographic bins. From those plots, we find that mean shear values for each field are about $|\gamma| \sim 10^{-3}$. In order to estimate the amplitude of the mean shear caused by the cosmic shear signal on scales larger than a field, we use a set of 2268 mock catalogs described in Appendix 4. For each field and for each tomographic sample from a mock catalog, we measure mean shear values. We repeat this measurement for each of the 2268 mock catalogs, and sort the mean shear values to find a 68.3% enclosing mean shear value below which 1549 mock samples are enclosed. The results for the combined sample of the four tomographic bins are shown in Figure 18 as the dashed-line circle for each field, with slightly different circle sizes for mean shear values of individual tomographic bins (see the caption of Figure 18 for more details). We note that the mean shear value expected from the intrinsic shape noise is $\sigma_e / \sqrt{N_g} \sim 0.3 / \sqrt{10^{6-7}} \sim O(10^{-4})$, where σ_e is the root-mean-square value of the intrinsic galaxy distortion (in shear units) and N_g is the number of galaxies. This value is much smaller than the mean shear from the mock catalogs, suggesting that the mean shear value is indeed dominated by cosmic shear that is coherent over

the field. We find from Figure 18 that most of the measured values are located within the 68.3% enclosing circle, which is consistent with the finding in Mandelbaum et al. (2018a). In fact, only the highest redshift tomographic bin of GAMA09H field has a mean shear beyond the 95.5% range ($|\gamma| = 3.0 \times 10^{-3}$ for this case).

In addition to the above test, we estimate a statistical significance of the measured mean shears against the null hypothesis that they arise solely from the cosmic shear as follows. Using the data set of mean shears measured from the tomographic mock catalogs, we derive the covariance matrix (see Appendix 4.1 for details), $\text{Cov}(d_i, d_j)$, where d_i is the data vector consisting of mean values of the two shear components in each of the four tomographic bin, namely $d_i = (\bar{\gamma}_1^1, \bar{\gamma}_1^2, \bar{\gamma}_1^3, \bar{\gamma}_1^4, \bar{\gamma}_2^1, \bar{\gamma}_2^2, \bar{\gamma}_2^3, \bar{\gamma}_2^4)$. Given this covariance matrix for each field, we compute χ^2 of the data relative to the null hypothesis; the results are summarized in Table 2 along with the corresponding p -values. The p -values are reasonable for all fields except the GAMA09H field, in which the p -value is slightly smaller than the conventional criterion of 0.05. However, since we measured the mean shear independently in six fields, the chances of getting one field with a p value less than 0.028 is $1 - 0.972^6 = 0.16$. Thus we conclude that the measured mean shears are consistent with that expected from large-scale cosmic shear.

Although we have found no clear evidence of additive shear bias arising from residual systematics, we check the impact of such a possible residual shear on our cosmological analysis by modeling it as a redshift-independent constant shear, which we denote as $\bar{\gamma}$. We expect that the redshift-independent constant shear is a reasonable assumption for the following reason. The redshift-dependence of shape measurements may arise from the difference of galaxy properties such as sizes between different redshifts, which are estimated as the selection biases, m_{sel}^a and m_R^a (see Section 2.3.1 and Section 5.7 of Hikage et al. 2019). We find that the variation in the redshift-dependent selection biases (to be specific $1 + m_{\text{sel}}^a + m_R^a$) among four tomographic bins is $\sim 2\%$ at largest (see Table 3 of Hikage et al. 2019). In our systematics tests in Sec. 5.2.3, we add $\bar{\gamma}$ to the *theoretical model* of ξ_+ , and than marginalize over $\bar{\gamma}$ to see how cosmological constraints change. We note that ξ_- is unaffected by this constant shear due to the cancellation between $\langle \gamma_t \gamma_t \rangle$ and $\langle \gamma_\times \gamma_\times \rangle$.

Appendix 2 PSF leakage and residual PSF model errors

In this Appendix, we examine the impact of PSF leakage and residual PSF model error on the measurement of shear correlation functions, employing the simple linear model as

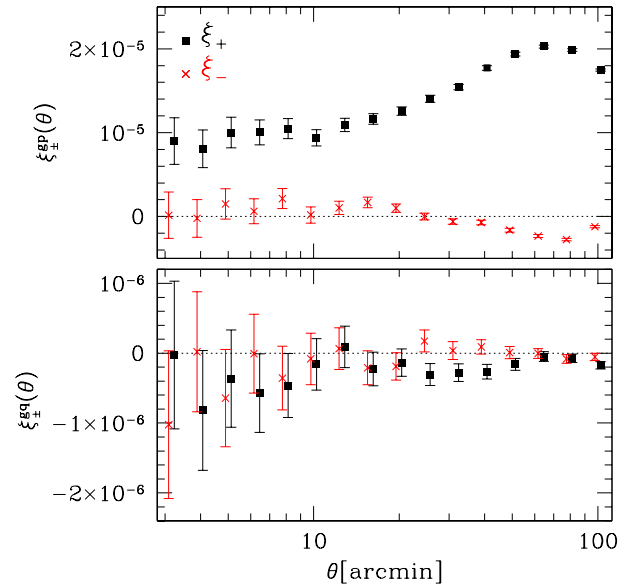


Fig. 19. Upper (bottom) panel shows the cross correlation function between galaxy shears and PSF shapes (difference in shapes between the PSF and stars) converted into shear. Filled squares and red crosses are for ξ_+ and ξ_- , respectively. In the bottom panel, points are horizontally shifted slightly for clarity. In measuring these signals, the combined catalog of the four tomographic redshift bins is used for the galaxy shear sample, and reserved stars (as described in Section 3.2) are used for the PSF sample.

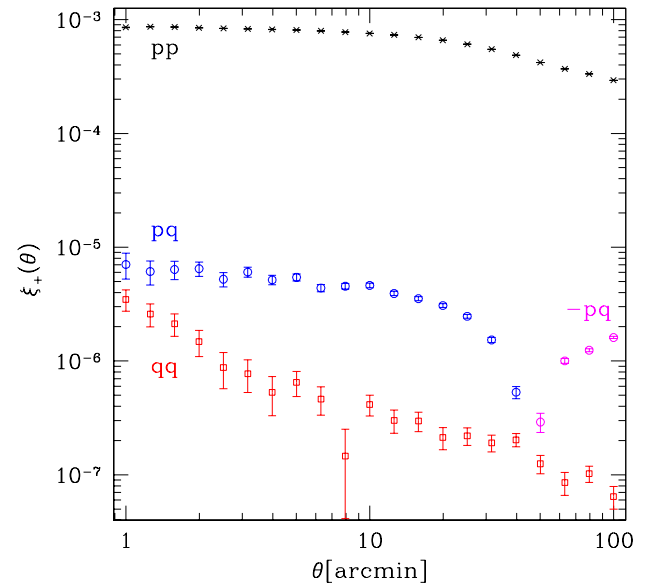


Fig. 20. The auto- and cross-correlation functions between PSF shapes (γ^p) and the difference between PSF and star shapes (γ^q), i.e., ξ_+^{pp} (black crosses), ξ_+^{pq} (red squares), and ξ_+^{pq} (blue bars for $\xi_+^{pq} > 0$, and magenta bars for $\xi_+^{pq} < 0$ plotted as $-\xi_+^{pq}$).

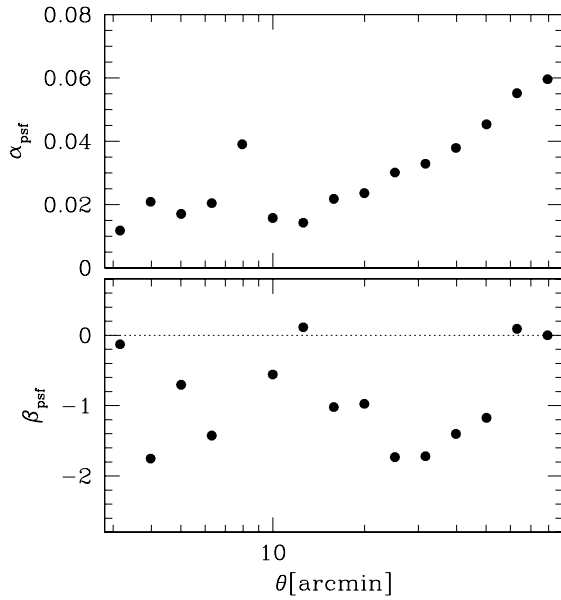


Fig. 21. Model parameters in PSF leakage and residual PSF model derived for ξ_+ using equations (A1) and (A2). Error bars, which largely come from errors on ξ_+^{gq} (see the lower panel of Figure 19), are not shown.

described in equations (6) and (7). The model parameters, α_{psf} and β_{psf} , can be estimated by the cross correlation functions between $\gamma^{p,q}$ and galaxy shears, $\xi^{gp,qq} = \langle \hat{\gamma}^{p,q} \rangle$, which are related to $\xi_{\pm}^{pp,pq,qq}$ as

$$\xi_{\pm}^{gp} = \alpha_{\text{psf}} \xi_{\pm}^{pp} + \beta_{\text{psf}} \xi_{\pm}^{pq}, \quad (\text{A1})$$

$$\xi_{\pm}^{gq} = \alpha_{\text{psf}} \xi_{\pm}^{pq} + \beta_{\text{psf}} \xi_{\pm}^{qq}. \quad (\text{A2})$$

In measuring these quantities, we use reserved stars, which are described in more detail in Section 3.2, for the PSF sample, and for the galaxy shear sample, we use the combined catalog of the four tomographic redshift bins, because the measurement of $\xi_{\pm}^{gp,qq}$ is very noisy as shown below. As a consequence, we do not take into account possible redshift dependence of α_{psf} and β_{psf} . See Section 4.2 of Hikage et al. (2019) for further discussions on this point.

We first consider the ξ_+ component. The measured $\xi_{\pm}^{gp,qq}$ are shown in Fig 19, where the error bars represent the shape noise. As shown in the upper panel, we obtain high signal-to-noise ratio detections for ξ_+^{gp} over a wide angular range. The signal-to-noise ratios for ξ_+^{gq} are marginal, but there is a clear trend toward negative values. Using these measured values, together with $\xi_+^{pp,pq,qq}$ shown in Figure 20, we derive α_{psf} and β_{psf} with equations (A1) and (A2). The results are shown in Figure 21, where we omit error bars which are dominated by errors on ξ_+^{gq} (see the lower panel of Figure 19). Taking the simple average and standard deviation of the 9 points in the angular range from $\sim 8'$ to $\sim 50'$, the range is used in the cosmo-

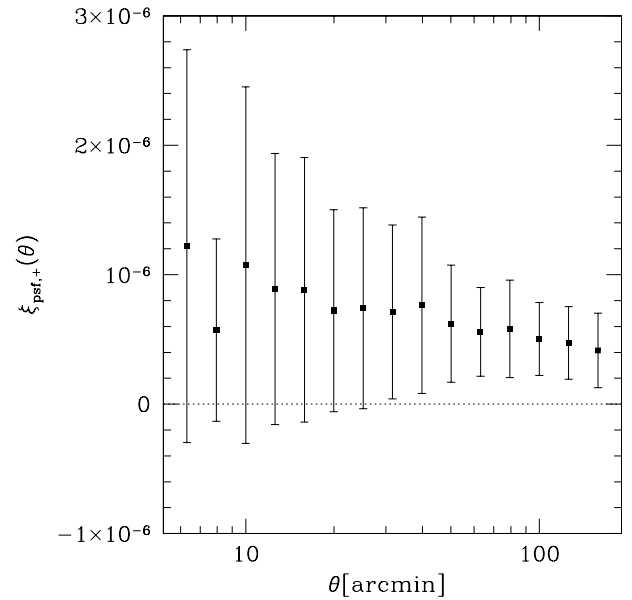


Fig. 22. $\xi_{\text{psf},+}$ defined in equation (7) is shown. Here we adopt $\alpha_{\text{psf}} = 0.029 \pm 0.010$ and $\beta_{\text{psf}} = -1.42 \pm 1.11$. Errors are computed from those of α_{psf} and β_{psf} .

logical analysis in this study, we find $\alpha_{\text{psf}} = 0.029 \pm 0.010$ and $\beta_{\text{psf}} = -1.42 \pm 1.11$, which we adopt as the prior ranges of these parameters. Hikage et al. (2019) derived the same quantities with the same data set but in the power spectrum analysis, and found $\alpha_{\text{psf}} = 0.057 \pm 0.018$ and $\beta_{\text{psf}} = -1.22 \pm 0.74$. There is a difference in the central values of α_{psf} , although they are marginally consistent with each other. This difference might reflect the different angular ranges between the two studies (see Appendix 5).

Using the derived parameter values, we compute an estimate of the impact of the PSF errors on ξ_+ , namely $\xi_{\text{psf},+}$ defined in equation (7). The result is shown in Figure 22, where error bars are computed from those of α_{psf} and β_{psf} . The derived $\xi_{\text{psf},+}$ should be considered as a rough estimate because it is based on the simple linear model, equations (6) and (7). Taking into account the large error bars, it is reasonable to conclude that $\xi_{\text{psf},+}$ is about 10^{-6} on scales $5' < \theta < 60'$.

Next we measure the ξ_- component. The measured $\xi_{\pm}^{pp,qp,qq}$ are shown in Figure 23 and $\xi_{\pm}^{gp,qq}$ are shown in Figure 19. The SNs are lower compared with the corresponding ξ_+ components, ξ_{\pm}^{gq} and ξ_{\pm}^{gq} are especially noisy. We thus cannot measure α_{psf} and β_{psf} from ξ_- alone. In order to examine the impact of PSF leakage and residual PSF model errors on the cosmic shear ξ_- , we employ the estimates from ξ_+ instead. Taking $\alpha_{\text{psf}} \sim 0.03$ and $\beta_{\text{psf}} \sim -1.4$, we find the additional PSF term in equation (7) is about -1×10^{-8} at $\theta \sim 1$ degree, which is more

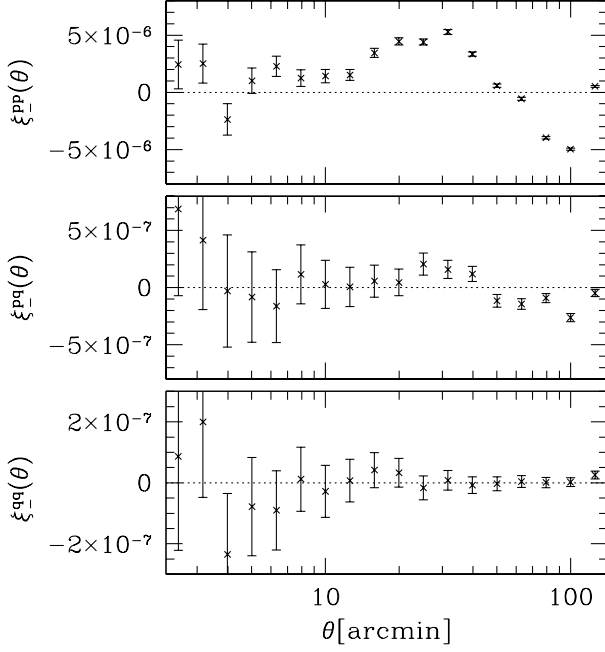


Fig. 23. From top to bottom panels, ξ_{PP}^{\pm} , ξ_{PQ}^{\pm} , and ξ_{QQ}^{\pm} are shown. See Section 3.1 for their definitions and details of measurements. Error bars represent the shape noise.

than two orders of magnitude smaller than the cosmic shear signals. Thus for ξ_{-} , we do not apply any correction for systematics caused by the residual PSF and PSF model.

Appendix 3 E/B-mode cosmic shear TPCFs

In this Appendix, we present E/B-mode (gradient/curl-mode) decomposition of the cosmic shear TPCFs (Crittenden et al. 2002). The purpose here is to test our assumption that the cosmic shear field we used for the cosmological analysis is consistent with being B-mode free as expected from gravitational lensing by a scalar gravitational field (Kaiser 1992). Note that the B-mode shear component in the HSC first year shear catalog was examined by Oguri et al. (2018) and Hikage et al. (2019): The former looked into the B-mode aperture mass map, whereas the latter used the cosmic shear power spectra in the multipole range of $300 < \ell < 1900$, and both concluded that the B-mode component is consistent with zero. Here we examine the E/B-mode tomographic shear TPCFs, allowing us to closely examine B-mode signals both for individual tomographic bins and for individual θ -bins of $\xi_{+}(\theta)$.

The E/B-mode shear TPCFs are given via ξ_{\pm} as

$$\xi_E(\theta) = \frac{\xi_{+}(\theta) + \xi'(\theta)}{2}, \quad (\text{A3})$$

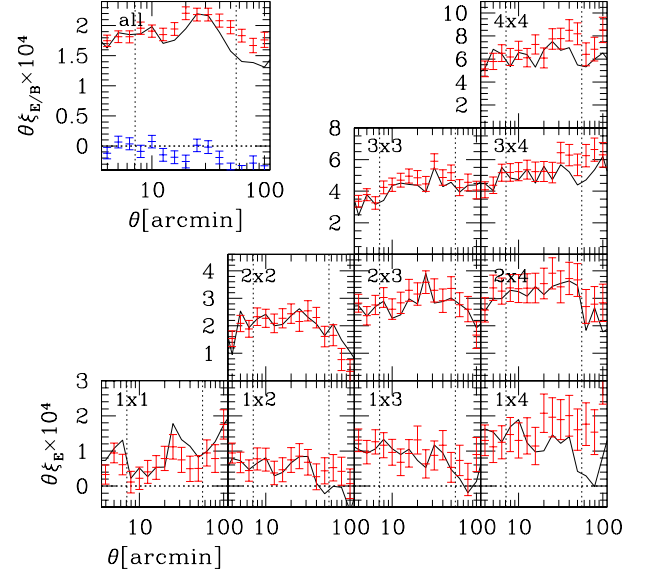


Fig. 24. Bottom right triangular tiled plots: The measured E-mode tomographic shear correlation function ξ_E (red bars with error bars) compared with ξ_{+} (black solid line). Combinations of tomographic redshift bins are labeled in each plot. Top left panel: E-mode (red symbols) and B-mode (blue symbols) non-tomographic (the galaxies in all four tomographic bins $0.3 < z < 1.5$ are combined) shear correlation functions. Error bars represent the shape noise for $\xi_{E/B}$. Vertical dotted lines show the angular range (for ξ_{+}) used for the cosmological analysis.

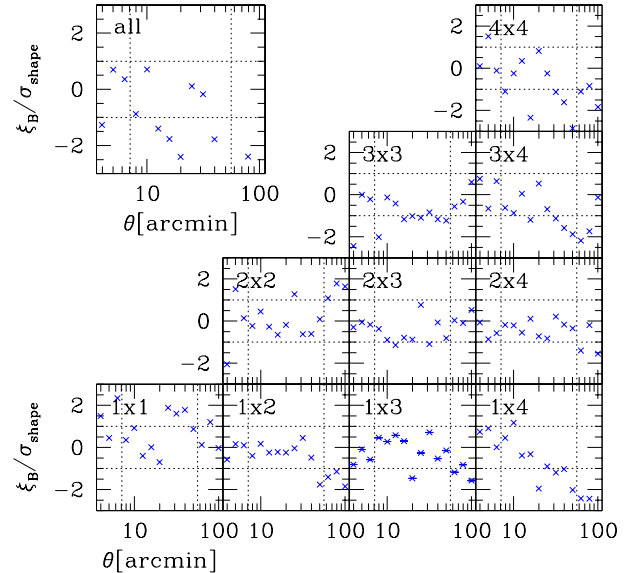


Fig. 25. Bottom right triangular tiled plots: The measured B-mode tomographic shear correlation function ξ_B normalized by the shape noise σ for ξ_B . Top left panel: B-mode non-tomographic shear correlation functions normalized by the shape noise. Vertical dotted lines show the angular range (for ξ_{+}) used for the cosmological analysis, whereas the horizontal dotted lines represent ± 1 .

$$\xi_B(\theta) = \frac{\xi_+(\theta) - \xi'_+(\theta)}{2}, \quad (\text{A4})$$

where

$$\xi'_+(\theta) = \xi_-(\theta) + 4 \int_{\theta}^{\infty} \frac{d\phi}{\phi} \xi_-(\phi) - 12\theta^2 \int_{\theta}^{\infty} \frac{d\phi}{\phi^3} \xi_-(\phi). \quad (\text{A5})$$

In the computation of the two integrals of equation (A5), we measure $\xi_-(\theta)$ in the θ -range $0'.16 \leq \theta \leq 416'$ in equal log-intervals of $\Delta \log \theta = 0.02$. In order to complete the integrals in equation (A5) beyond $\theta = 416'$, we use the theoretical model with the WMAP9 Λ CDM cosmology (Hinshaw et al. 2013). The result is not sensitive to the choice of the cosmological model for the angular range we adopt for ξ_+ ($7'.1 \leq \theta \leq 56'$).

The measured E/B-mode TPCFs are shown in Figures 24 and 25, where the error bars represent the shape noise for $\xi_{E/B}$. In order to evaluate the significance of the B-mode, we compute the standard χ^2 value for the null signal, for tomographic B-mode TPCFs with the shape covariance estimated from the data. We adopt the angular range of our fiducial choice for ξ_+ , which is shown with dotted vertical lines in Figure 25, and we combine all 10 tomographic combinations. We find $\chi^2 = 85.1$ for $N_d = 90$, leading to a p -value of 0.63. Therefore we safely conclude that no evidence for a significant B-mode shear is found.

Appendix 4 Mock simulation data

Here we describe the HSC mock shape catalogs, focusing on aspects which are directly relevant to this study. See Shirasaki et al. (2019) for a full description of how the mock data were constructed, and a comprehensive study of the covariance matrix.

Mock catalogs are constructed based on 108 realizations of the full-sky gravitational lensing ray-tracing simulation through a large set of cosmological N -body simulations (Takahashi et al. 2017)⁷. The simulations adopt a flat Λ CDM cosmology which is consistent with the WMAP9 cosmology (Hinshaw et al. 2013) with $\Omega_c = 0.233$, $\Omega_b = 0.046$, the total matter density $\Omega_m = \Omega_c + \Omega_b = 0.279$, $\Omega_\Lambda = 1 - \Omega_m = 0.721$, $h = 0.7$, $\sigma_8 = 0.82$, and $n_s = 0.97$. The lensing data (convergence and shear) are computed on HEALPix (Górski et al. 2005) format grids with a grid spacing of $0'.42$, and on 38 source planes with a regular radial interval of comoving $150h^{-1}$ Mpc. The most distant source plane is located at $z = 5.3$. The degree of independence in 108 full-sky realizations has been studied in Shirasaki et al. (2017), who show that the 108 full-sky maps can be safely regarded as independent realizations.

⁷ The full-sky light-cone simulation data are freely available for download at http://cosmo.phys.hirosaki-u.ac.jp/takahasi/allsky_raytracing/.

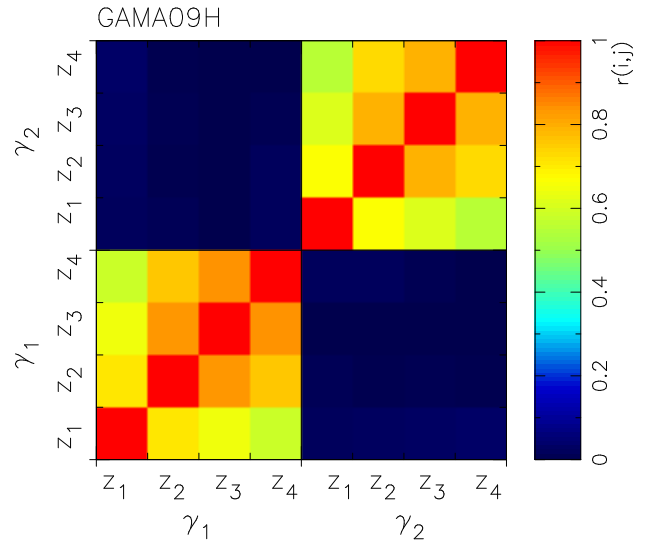


Fig. 26. Two-dimensional matrix plot showing the correlation coefficient of the mean shear covariance matrix, $r(d_i, d_j) = \text{Cov}(d_i, d_j) / \sqrt{\text{Cov}(d_i, d_i) \text{Cov}(d_j, d_j)}$. Here we show the result for the GAMA09H field, but results in the other fields are almost identical to this.

From each full-sky lensing data, 21 non-overlapping HSC footprints are taken, yielding a total of $21 \times 108 = 2268$ independent mock samples. Here we briefly describe the procedure for constructing HSC mock shape catalogs, referring interested readers to Shirasaki et al. (2019), Shirasaki & Yoshida (2014), Shirasaki et al. (2017), and Oguri et al. (2018) for more details. For each mock realization, galaxy positions are taken from the real HSC shape catalog to keep exactly the same survey geometry including masked regions. The same tomographic redshift sampling as the real sample is made based on the same point estimator of photo- z 's. The redshift of each galaxy is drawn randomly according to the photo- z PDF $P(z)$ for each mock realization. The intrinsic galaxy shape and shape measurement noise are taken from the two component distortion (e_1, e_2) of the real HSC shape catalog (an estimate of measurement noise is also given in the catalog) but a random rotation is applied to erase the cosmic shear signal in the real catalog. This allows us to preserve both the intrinsic shape noise and measurement noise in the statistical sense. Finally, the lensing shear and convergence are taken from full-sky simulation data for each galaxy, and mock distortion data, (e_1, e_2), were computed using the relationship between the observed (i.e., lensed) and intrinsic galaxy shapes under the action of gravitational lensing (e.g., Miralda-Escude 1991; Bernstein & Jarvis 2002).

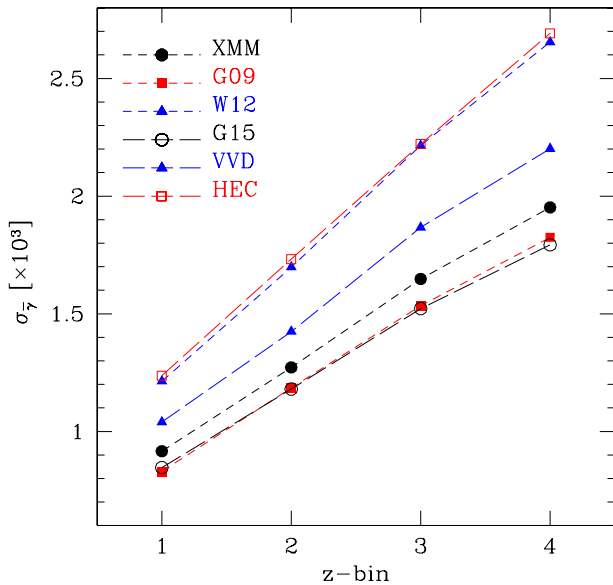


Fig. 27. The root-mean-square values of two component mean shears derived from the diagonal components of the covariance matrix, i.e., $\sigma_{\bar{\gamma}}^a = [\text{Cov}(\bar{\gamma}_1^a, \bar{\gamma}_1^a) + \text{Cov}(\bar{\gamma}_2^a, \bar{\gamma}_2^a)]^{1/2}$.

A.4.1 Covariance of mean shears over fields

A mean shear over a field can naturally arise from the gravitational lensing shear effect on scales larger than the field, and also can arise from residual systematics in shear estimation and/or image processing. The latter, if exists, can have an influence on the cosmological inference. In Appendix 1, we utilize the mock catalogs to check if the measured mean shears over each field in the real HSC shape catalog are consistent with the cosmic shear origin. Here we describe the covariance matrix of mean shears which is used in this test.

We compute the mean shear of mock catalogs for each field and for each tomographic sample. It is computed by a simple mean with the shear weight (w), $\bar{\gamma}_i^a = \sum w \gamma_i / \sum w$, where the subscript i denotes the two shear components, the superscript a denotes the tomographic bins, and the summation runs over all galaxies in each tomographic sample and field. We then define the data vector consisting of eight mean shear components,

$$d_i = (\bar{\gamma}_1^1, \bar{\gamma}_1^2, \bar{\gamma}_1^3, \bar{\gamma}_1^4, \bar{\gamma}_2^1, \bar{\gamma}_2^2, \bar{\gamma}_2^3, \bar{\gamma}_2^4). \quad (\text{A6})$$

Finally, for each field we compute the covariance matrix of the data vector using 2268 mock realizations, denoted by $\text{Cov}(d_i, d_j)$. Figure 26 shows the correlation coefficients of the covariance matrix, $r(d_i, d_j) = \text{Cov}(d_i, d_j) / \sqrt{\text{Cov}(d_i, d_i) \text{Cov}(d_j, d_j)}$ for the GAMA09H field as an example. We find that the mean shears in different tomographic bins are strongly correlated. This is

the natural consequence of galaxies at different redshifts being affected by the same large-scale structure along the line-of-sight. We also find that the correlation is tighter for closer tomographic redshift bins. Figure 27 shows the root-mean-square values of two component mean shears derived from the diagonal components of the covariance matrix, i.e., $\sigma_{\bar{\gamma}}^a = [\text{Cov}(\bar{\gamma}_1^a, \bar{\gamma}_1^a) + \text{Cov}(\bar{\gamma}_2^a, \bar{\gamma}_2^a)]^{1/2}$. As expected, the root-mean-square value is higher for the higher redshift tomographic bins, as the gravitational lensing effect is stronger for sources at higher redshifts. The difference in the root-mean-square values among different fields is due to the different field areas. It is important to note that the expected value of the mean cosmic shear over a field depends on the cosmological model, and thus the covariance also does. The root-mean-square values presented here are for the WMAP9 cosmology adopted in the mock simulations.

Appendix 5 Connection with the power spectrum analysis

In this study, we used exactly the same tomographic galaxy samples as those used in Hikage et al. (2019), but that study adopted Fourier-space power spectra as rather than the real space TPCFs used in this paper. Here we compare the information content in the measured cosmic shear statistics between two studies.

To do so, we divide the ℓ -integration range of the TPCFs into three parts (see equation 5); $\ell < 300$, $300 < \ell < 1900$, and $\ell > 1900$. The second ℓ range corresponds to the range adopted in Hikage et al. (2019) for their cosmological analysis. We evaluate these partial contributions assuming the WMAP9 cosmology and compute the fractions to the total TPCFs defined by $\xi_{\pm}(\theta, \ell_{\min} < \ell < \ell_{\max}) / \xi_{\pm}(\theta)$. The results are shown in Figure 28, in which we show the result only for one combination of tomographic bins, as we find that the results are quite similar for different combinations of tomographic bins. On the angular range used in this study, the dominant contribution to ξ_+ comes from $\ell < 300$, especially on larger θ scales. For ξ_+ , on scales $\theta < 60'$, the major contribution comes from $300 < \ell < 1900$, whereas on larger scales the majority of the contribution comes from $\ell < 300$. To summarize, a large part of the contribution to ξ_{\pm} on scales adopted in this study comes from $\ell < 300$, which was not used in the cosmic shear power spectrum analysis in Hikage et al. (2019).

We also evaluate the fractional contribution to the total signal-to-noise ratio from the above three ℓ ranges. We define the partial signal-to-noise ratio as

$$S/N^{\ell\text{-part}} = \sum_{i,j} d_i(\xi_{\pm}^{\ell\text{-part}}) \text{Cov}_{ij}^{-1} d_j(\xi_{\pm}), \quad (\text{A7})$$

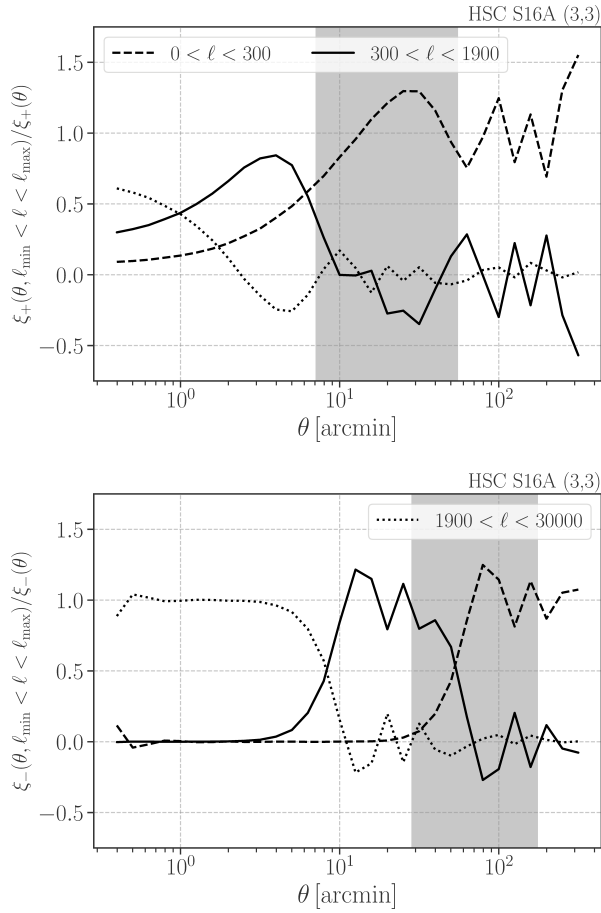


Fig. 28. The fractional contributions of ξ_{\pm} coming from three disjoint ℓ -ranges are shown; dashed lines for $\ell < 300$, solid lines for $300 < \ell < 1900$, and dotted lines for $1900 < \ell < 30000$. Only the auto correlation in the third tomographic bin, ξ_{\pm}^{33} , are plotted, but the results are similar for a different combination of tomographic bins. Gray regions show the angular ranges used in this study.

where $\xi_{\pm}^{\ell\text{-part}}$ is the TPCFs computed from a limited ℓ -range. Again we assume the *WMAP9* cosmology and adopt the same angular bins for the data vector d_i and covariance matrix as those used in the actual cosmological analysis in this study. We find that the fractional contributions to the total S/N are 57% ($\ell < 300$), 37% ($300 < \ell < 1900$), and 6% ($\ell > 1900$). It follows that, although Hikage et al. (2019) and this study share the same dataset, in deriving cosmological constraints two studies utilize fairly different and complementary information. This also explains the relatively weak correlations of cosmological constraints derived from power spectrum and TPCF analyses when analyzing the same mock catalogs (see Section 6.7). Note that the mock analysis presented in Section 6.7 uses the realistic mock catalogs in which the realistic shape noise and redshift distributions of galaxies are included. We performed this test, instead of a noise-less test, to experimentally ex-

amine the correlations between the two analyses in the presence of such realistic noises. Nevertheless, a noise-less test would be valuable to examine a more theoretical aspect of the information content in the real/Fourier-space cosmic shear measurements, which we leave for a future study.

Appendix 6 On an error in a constraint on S_8 caused by uncertainties in galaxy redshift distributions

Here we derive a relationship between an uncertainty in a galaxy redshift distribution and an error in a constraint on S_8 induced by it in an approximative but reasonably reliable manner. Then we use the derived relationship to discuss a possible impact of an error in the outlier fraction of galaxy redshift distributions on a constraint on S_8 .

Since the constraint on S_8 primary comes from the amplitude of the cosmic shear correlation function (or power spectrum) on linear to quasi-nonlinear scales, we will focus on $\xi_+(\theta)$ at $\theta = 10$ arcmin. For simplicity, we will not treat the full galaxy redshift distribution but characterize the distribution with a single parameter, the mean redshift denoted by \bar{z}_s . We consider $\xi_+(\theta = 10')$ for a single source plane model (that is $p(z) = \delta_D(z - \bar{z}_s)$, where δ_D is the Dirac's delta function). The relation between $\xi_+(\theta = 10')$ and \bar{z}_s can be approximated by the following power-law relation with good accuracy, $\xi_+(\theta = 10') \propto \bar{z}_s^u$ with $u \simeq 2.0$ (1.8) for $0.1 < \bar{z}_s < 0.7$ ($0.7 < \bar{z}_s < 1.5$). Also we find an accurate power-law relation with S_8 (for a range of $0.4 < S_8 < 1.2$), $\xi_+(\theta = 10') \propto S_8^v$ with $v \simeq 2.8, 2.3, 2.0$, and 1.8 for $\bar{z}_s = 0.44, 0.77, 1.05$, and 1.33, respectively. From those two scaling relations, we have the following relationship,

$$\frac{\delta S_8}{S_8} = -\frac{u}{v} \frac{\delta \bar{z}_s}{\bar{z}_s}. \quad (\text{A8})$$

Note that the scaling factor u/v ranges from 0.7 to 1 for our interested range of $0.4 \lesssim \bar{z}_s \lesssim 1.4$. It is also noted that the anti-relationship originates from the fact that an over/under-estimate of the mean redshift leads to an over/under-estimate of the theoretical prediction, resulting in an under/over-estimate of S_8 to compensate.

In the re-analysis of DES-Y1 cosmic shear data presented in Joudaki et al. (2019), it is reported that the mean redshifts of the galaxy redshift distributions derived bases on the COSMOS 30-band photo- z are systematically lower than those derived based on spectroscopic samples. They found $\Delta \bar{z}_s$ (defined by $\bar{z}_s[\text{spec-}z] - \bar{z}_s[\text{COSMOS-30}]$) of +0.014, +0.053, +0.020, and +0.035 for their four tomographic redshift bins ($0.2 < z < 0.43$, $0.43 < z < 0.63$, $0.63 < z < 0.9$, and $0.9 < z < 1.3$). They found the best

fit S_8 values of 0.763 and 0.793 for galaxy redshift distributions based on the COSMOS 30-band photo- z and spectroscopic samples, respectively, resulting in $\Delta S_8 = S_8[\text{spec-}z] - S_8[\text{COSMOS-30}] = -0.030$. The relation between those values are in a good agreement with one expected from the derived relationship, equation (A8), supporting its validity.

Finally, we discuss a possible impact of an error in the outlier fraction of galaxy redshift distributions on a constraint on S_8 using simple models. Suppose a galaxy redshift distribution has a bi-modal shape, such as one shown in top-panel of Figure 1, consisting of a main population with $\langle z_{\text{main}} \rangle = 0.5$ and an outlier population with $\langle z_{\text{out}} \rangle = 3$. Assuming the outlier fraction of 5%, the mean redshift of this distribution is $\bar{z}_s = 0.95 \times 0.5 + 0.05 \times 3 = 0.625$. If we suppose 10% error in the outlier fraction, the error in the mean redshift is $\delta \bar{z}_s = \pm 0.0125$, leading to $\delta S_8 \simeq \mp 0.016$ (here we used equation (A8) with $u/v = 0.8$). Actual errors in the outlier fraction of our galaxy samples are not understood well, but this rough estimate gives us a crude idea of its possible impact on a constraint on S_8 .